J. Fluid Mech. (1988), *vol.* 194, *pp.* 511–547
Printed in Great Britain

The repeated filamentation of two-dimensional vorticity interfaces

By DAVID G. DRITSCHEL

Department of Applied Mathematics and Theoretical Physics, University of Cambridge, Silver Street, Cambridge CB3 9EW, UK

(Received 20 May 1987 and in revised form 28 January 1988)

Undular disturbances of *arbitrarily small steepness* to the boundary of a circular patch of uniform vorticity are found to give way to a qualitatively different type of behaviour after a time inversely proportional to the initial wave steepness squared. Repeatedly, thin filaments are drawn out at a frequency of nearly half the vorticity jump across the interface (the intrinsic frequency of linear waves on the interface), and the interaction between the filaments and the undulating boundary generate new disturbances from which still greater numbers of filaments of increasingly complicated shape are drawn out. The vortex boundary thereby experiences an extraordinary, continual and apparently irreversible growth in complexity.

Essentially the same phenomenon occurs on all vortex-patch equilibria, e.g. the Kirchhoff elliptical vortex, with even greater complexity. The steepening of a disturbance on a non-circular vortex proceeds faster than that on a circular vortex, because of the varying mean strain and shear seen by the disturbance as it travels around the vortex boundary.

Generalizations to more than one vorticity interface, to flows on the surface of a sphere, and to sharp but not infinitely sharp vorticity gradients are also discussed. The results support the view that almost any two-dimensional, inviscid, incompressible flow with large vorticity gradients will exhibit repeated filamentation.

1. Introduction

In the last century, Thomson (1880) proved linear stability for a column of uniform axial vorticity in an unbounded, inviscid, incompressible and otherwise motionless fluid. Linear stability, however, does not sufficiently constrain the evolution of finite-amplitude disturbances, and to this day the vortex is not known to be stable in this nonlinear sense.

Several results bearing upon the fate of finite-amplitude disturbances have recently been brought forward by Wan & Pulvirenti (1985) and Dritschel (1988*a*). They considered the simpler two-dimensional problem, the so-called vortex-patch problem, and found that small but finite boundary disturbances cannot significantly disrupt the gross shape of the vortex. The degree of disruption is measured by a norm, and a (Liapunov) stability theorem is a statement on the maximum growth of that norm over all time. Wan & Pulvirenti used the L^1 area norm (the magnitude of the areal displacement of the vortex boundary from its equilibrium position) to prove stability (but in a non-standard sense; for their theorem see equation (1) of Dritschel (1988*a*) and see also §5 of that paper). Dritschel proved (Liapunov) stability in terms of the mean-square y-displacement of the vortex boundary (here y is equal to half of

the radius squared). Viewed in this norm, the disturbance neither grows nor decays, because the norm is constant in time.

Although these stability results prevent small disturbances from altering the gross shape of the vortex by more than a correspondingly small amount, they say nothing about the possible changes in the detailed structure of the vortex boundary over time. For instance, there are no nonlinear stability theorems that bound the mean-quartic displacement of the vortex boundary. The results below illustrate that extraordinary nonlinear behaviour eventually develops from gentle undular disturbances, behaviour transparent to the norms used in the proofs of stability above.

The initial stages of this nonlinear behaviour were calculated by Deem & Zabusky (1978, figure 4) using an early 'contour dynamics' algorithm (an algorithm specifically designed for piecewise-constant vorticity distributions). That calculation indicated that a circular vortex with a smooth initial disturbance eventually ejects a thin filament of vorticity having a peak curvature at its tip many times greater than the initial peak curvature along the vortex boundary. However, owing to insufficient resolution, and, in particular, owing to the difficulty in properly resolving the filament, their calculation could not be continued further. A systematic study was later conducted by Pullin (1981) to determine the conditions for and nature of filament formation on a discontinuous vorticity interface running parallel to a rigid wall. He found that sufficiently steep initial disturbances lead to the formation of a filament, within a time equal to two oscillations of the disturbance in linear theory. The integration times were limited by the low spatial resolution employed and, when a filament formed, by the inability of his numerical algorithm to continue. Significantly, Pullin saw the possibility that filaments might be generated repeatedly, with a period equal to the linear disturbance period.

More recently, Stern (1985) and Stern & Pratt (1985) have re-examined filament formation on interfaces of discontinuous vorticity. Both studies claim to consider interfaces of infinite length (numerically approximated), the first in the absence of rigid boundaries, and the second in the presence of a rigid wall. In the latter case, the distance of the interface from the wall differs on either 'end' of the interface. On the basis of their numerical calculations, done at low resolution and for short times, Stern (1985) and Stern & Pratt (1985) concluded, apparently prematurely, that there exists a finite steepness below which a disturbance will never lead to the formation of a filament. The results of the present paper, which are based on high-resolution numerical experiments *and* on a mathematical analysis of the governing equations in the limit of shallow disturbances, on the contrary support the view that disturbances of arbitrarily small steepness eventually lead to the formation of not just one filament, but an apparently endless succession of filaments of increasingly complicated shapes.

The present paper examines the process of 'filamentation' from a combined numerical–analytical perspective. The numerics is provided by a recent enhancement and overhaul of the contour dynamics method called 'contour surgery' (Dritschel 1988*b*, *c*, and briefly reviewed in the following section). This algorithm is designed to automatically remove vorticity features smaller than a prescribed scale and to efficiently redistribute resolution to maintain accuracy. In §3, filamentation is demonstrated numerically for disturbances to circular vortices, both in the planar and spherical (Dritschel 1988*c*) cases. Section 4 presents a weakly nonlinear theory which is shown to agree closely with the fully nonlinear calculations of §3 before the onset of filamentation. It is this that establishes the inevitability of filamentation

even for arbitrarily gentle initial undulations. Section 5 extends the results of §4 to non-circular vortices. First, a calculation of the filamentation of an elliptical vortex boundary illustrates the new features of strain and variable shear that generally hasten steepening and increase the complexity of filamentation. With the support of Appendix B, the section continues by proving that sufficiently small disturbances to the contours of general piecewise-constant vorticity flows obey a fully nonlinear equation for the evolution of a disturbance to an infinitely straight vorticity interface, but with coefficients dependent on the time variation of strain and shear along the basic-state vorticity interface. Then, just as in §4, a weakly nonlinear equation is derived, whose form of evolution is now, however, dependent only on the shape of the initial disturbance and on an integral measure of the strain and shear along the basic-state, supporting interface. In §6, sharp but finite gradients of vorticity are examined. Disturbances whose amplitudes are comparable to the width of the high-gradient region are found to show marked differences in their evolution compared with similar disturbances to much sharper gradients. The paper concludes in §7 by interpreting the phenomenon of filamentation in the larger context of Rossby wave breaking (McIntyre & Palmer 1983, 1984, 1985) with applications to the Earth's stratosphere (Juckes & McIntyre 1987).

2. Numerics

The basic fluid system, assumed to be inviscid, incompressible, unforced, and free from all boundaries, satisfies, in the case of piecewise-constant vorticity, the following Lagrangian set of equations for the positions of the particles $\boldsymbol{x}$ on the interfaces of vorticity discontinuity, $C_k, k = 1, \ldots, N$:

$$\frac{\mathrm{d}\boldsymbol{x}}{\mathrm{d}t} = -\frac{1}{2\pi} \sum_{k=1}^{N} \tilde{\omega}_k \oint_{C_k} \log|\boldsymbol{x} - \boldsymbol{X}_k| \, \mathrm{d}\boldsymbol{X}_k, \tag{1}$$

where $\tilde{\omega}_k$ is the jump in vorticity crossing C_k inwards and $\boldsymbol{X}_k$ is a point on the boundary of C_k traversed leaving the interior of C_k on the left (Deem & Zabusky 1978; Zabusky, Hughes & Roberts 1979). We note in passing that (1) is true not only for flow on the infinite plane, but also flow on the surface of a sphere, only $\boldsymbol{x}$ and $\boldsymbol{X}_k$ are to be regarded as three-dimensional vectors stemming from the centre of the sphere and terminating at the surface of the sphere (Dritschel 1988*c*).

Numerical solutions to (1) are obtained using the 'contour surgery' technique in both the planar and spherical cases (Dritschel 1988*b*, *c*). Like contour dynamics, contour surgery replaces the continuous system (1) by an approximate finite discrete system. This approximation, of course, introduces errors that grow secularly in time. Accurate, extended integrations meant to capture detailed aspects of the development of disturbances on contours (e.g. filamentation) therefore require very high resolution.

Contour surgery is not simply a sophisticated version of contour dynamics, and some form of contour surgery is necessary to allow calculations to proceed, for example, beyond the formation of a single filament. The algorithm *automatically* removes vorticity features smaller than a predefined cutoff scale δ, in effect, forcing a maximum resolution. Surgery is not viscous dissipation, it is simply a way of controlling the rapid formation of small scales. In practice, one chooses δ sufficiently small that surgical errors are comparable with errors in spatial and temporal discretization (further discussion may be found in §4 of Dritschel 1988*b*). Spatial

discretization is controlled by two parameters (other than δ). The first, L, represents a typical large-scale length ($L = 1$ is taken throughout) while the second, μ, enters through the following approximate formula for the distance between adjacent nodes (enforced at each time step): $e = \mu(\bar{\kappa}L)^{-\frac{2}{3}}$, $\bar{\kappa}$ being a *non-local* curvature sensitive to the presence of nearby regions of high curvature on the same or different contours (vorticity interfaces). Finally, temporal discretization uses a fourth-order Runga–Kutta method with a time step, in the present paper, of $\Delta t = 0.05$ corresponding to a peak vorticity magnitude of $\omega_m = 2\pi$. The sensitivity of accuracy to variations in these parameters is discussed at length in Dritschel (1988*b*).

The accuracy of the calculations presented in this paper is measured by a single parameter, ϵ_C (in the planar case, see equation (15) of Dritschel 1988*b*; in the spherical case, see equation (A 5) of Dritschel 1988*c*). This parameter monitors the accumulation of phase error (the error in the orientation of the large-scale flow) over the course of the calculation. Of course, preferable measures of accuracy are reproducibility and reversibility, which, however, are not demonstrated in the present paper. Some such demonstrations are provided by Dritschel (1988*b*). It is fair to say, though, that numerous background calculations were performed to determine the resolution required for the experiments shown in this paper, some of which, owing to insufficient resolution, artificially delayed filamentation or altogether suppressed it.

3. Filamentation of circular vortices

In this section, numerical experiments are described that track the temporal development of initially gentle undular disturbances to circular vortices lying on the plane or on the surface of a sphere. The experiments illustrate both the qualitative and quantitative variation in the character of filamentation with the initial condition and the geometry.

The numerical calculations begin with a circular vortex (which is a spherical cap in spherical geometry) perturbed by weakly distorting a small part of the vortex boundary (see figure 1). In the planar case, the perturbation shifts the vortex boundary from $r = 1$ to $r = 1 + \rho(\theta, t = 0)$ where

$$\begin{aligned} \rho(\theta, 0) &= a\, \mathrm{e}^{-\frac{1}{2}(\theta/\theta_0)^2} && \text{symmetric case,} \\ &= -a(\theta/\theta_0)\, \mathrm{e}^{-\frac{1}{2}(\theta/\theta_0)^2} && \text{antisymmetric case,} \end{aligned} \tag{2}$$

for $-\pi \leqslant \theta \leqslant \pi$. a represents the (small) amplitude and $\theta_0 = \pi/m$, m integer, the (small) initial extent of the disturbance.

On the unit sphere, the perturbation shifts the *axial* position of the circular boundary from $z = z_0$, $-1 < z_0 < 1$, to $z = z_0 - r_0^2\rho(\theta, 0)$ with $r_0^2 = 1 - z_0^2$ and $\rho(\theta, 0)$ as given in (2). This choice of perturbation reduces (approximately) to the planar case as $z_0 \to 1$ when $a \ll 1$; since $r^2 + z^2 = 1$ on the sphere, $r/r_0 = (1 + 2\rho)^{\frac{1}{2}} = 1 + \rho + O(\rho^2)$ as $z_0 \to 1$ or, equivalently, as $r_0 \to 0$.

The evolution of a disturbance is most easily visualized in a frame of reference that brings particles on the equilibrium vortex boundary to rest, a frame that rotates at the uniform rate $\Omega = \frac{1}{2}\omega$ where $\omega = 2\pi$ is the jump in vorticity across the boundary. Only part of the vortex boundary is shown, from point A to B in figure 1, in such a way that point A always appears on the left-hand edge and point B on the right. Plotted is the disturbance $\rho(\theta, t)$ ($r(\theta, t) - 1$ in the planar case and $(z_0 - z(\theta, t))/r_0^2$ in the spherical one) every eighth of the rotation period, $T_p = 4\pi/\omega = 2$.

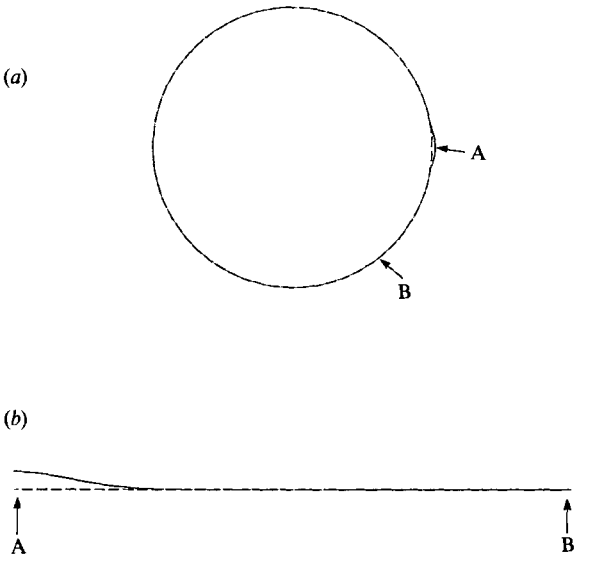

FIGURE 1. (*a*) A typical initial disturbance to a circular vortex on the plane or the sphere after stereographic projection. (*b*) The section from A to B in (*a*) as seen in the numerical calculations throughout the paper. The angular extent of the section may vary from calculation to calculation in order to focus attention on the disturbance evolution.

Figure 2 displays a planar calculation starting from antisymmetric initial conditions ($a = 0.025$, $m = 40$). At the beginning, one observes a nearly periodic repetition of the initial condition with a period of T_p (explained in the following section). A little after 6 periods, the character of the disturbance changes qualitatively. Filamentation commences at $t = t_f \approx 12.6$ with the formation of the first filament. Filamentation immediately follows the formation of infinite wave steepness, that is to say when part of the contour is vertical, and for this reason it is convenient to define t_f as the time when infinite wave steepness is reached. This stage of the evolution has been reported by other researchers (Deem & Zabusky 1978; Pullin 1981; Stern 1985; Stern & Pratt 1985, among others), but the subsequent evolution, in which filaments are repeatedly drawn out of the interface, has never been seen before (see figures 3 and 4 for close-up views at the beginning of filamentation and near the end of the calculation). The period of filament generation nearly equals that of the undular disturbance in linear theory, T_p. Note how the filaments towards the end of the calculation excite additional disturbances along the vortex boundary. These disturbances add to the growing complexity of the flow by steepening and producing filaments themselves.

The previous calculation began with an antisymmetric disturbance. Altering only the symmetry of the initial disturbance, by making it symmetric, one finds that the evolution qualitatively parallels that just described. The only notable difference is that the steepening takes longer, $t_f \approx 19.75$.

On the sphere, however, the form of filamentation qualitatively varies as a function of the mean axial position of the vortex. The most extreme case is when the vortex occupies an entire hemisphere ($z_0 = 0$, see figure 5). Filamentation begins at $t = t_f \approx 20.9$ and then, unlike the planar calculation illustrated above, filaments are alternately sent to either side of the mean position of the vortex boundary (see figure 6 for a close-up late in the evolution). This difference between the planar and

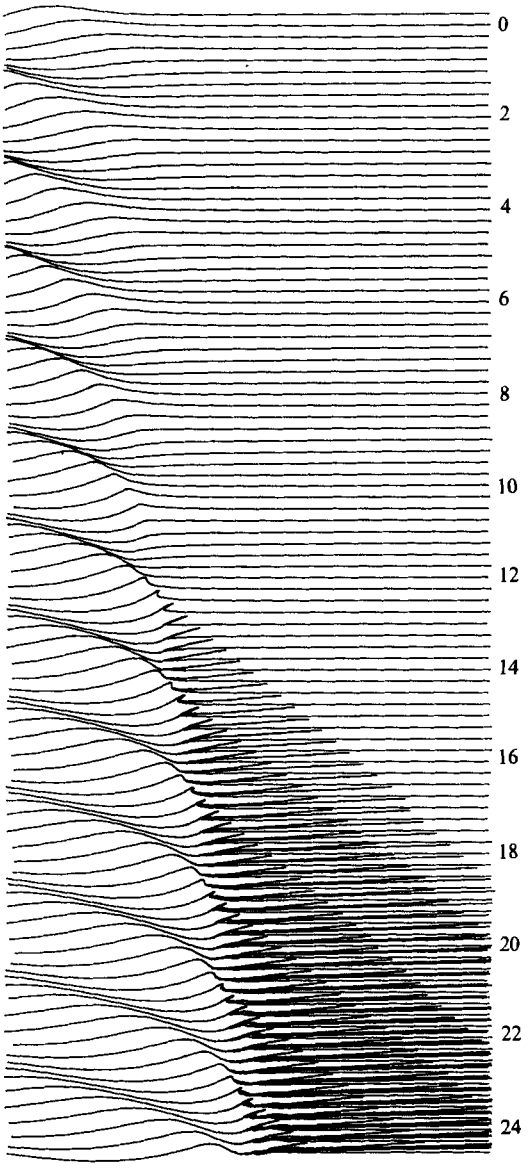

FIGURE 2. The evolution of an initially antisymmetric disturbance to a circular vortex on the plane (consult table 1 for numerical parameters and diagnostics; this is case 13). Time, labelled every 2 units, increases uniformly downwards.

hemispherical calculations is a consequence of the shear associated with the equilibrium vortices in the two cases. In the planar case, the shear is all on the outside of the vortex (the inside, in equilibrium, simply rigidly rotates). In the spherical case, however, the shear is of equal magnitude but opposite sign on the inside and outside of the vortex, because the vorticity in the lower hemisphere is just the opposite of that in the upper hemisphere.

When the equilibrium vortex is situated midway between the pole and the equator ($z = \sqrt{2}/2$), the shear is neither all to one side nor equal in magnitude on the inside and outside of the vortex (see figure 7). The evolution, however, resembles the planar

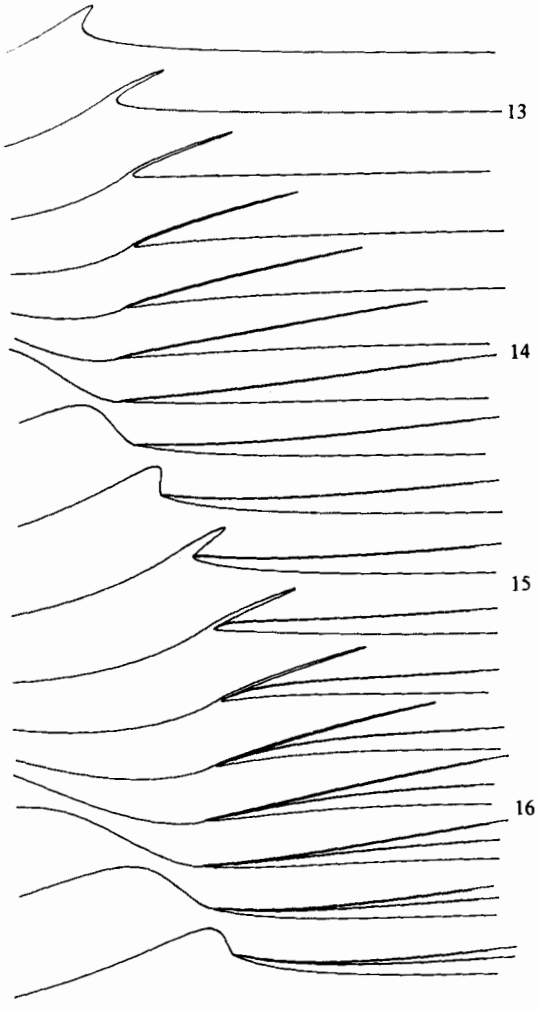

FIGURE 3. An enlarged view of part of figure 2 at the onset of filamentation, between $t = 12.75$ and 16.75.

case more than the equatorial one. It takes a value of z_0 between 0.25 and 0.5 to generate filaments on both sides (these calculations are not listed in table 1).

So far, we have seen that the 'sphericity' z_0 is the only parameter that qualitatively alters the form of filamentation. The other parameters which specify the amplitude, shape and symmetry of the initial disturbance may delay or speed up the steepening of the disturbance, but these parameters do not affect the qualitative nature of the evolution after filamentation commences.

The remainder of this section examines the dependence of the filamentation time t_f on the parameters a, θ_0, z_0 and symmetry. Table 1 lists the calculations performed, algorithm parameters for each, and several diagnostics including a measure of accuracy.

First, consider variations of the disturbance amplitude a with fixed $\theta_0 = \pi/40$ and $z_0 = 0$ (equatorial vortices). Figure 8 displays t_f versus $(40a)^{-2}$ for $a = (2/3)^{\frac{1}{2}}/40$, $1/40$ and $\sqrt{2}/40$ from which it appears that $t_f \propto a^{-2}$ for both symmetric and antisymmetric initial conditions.

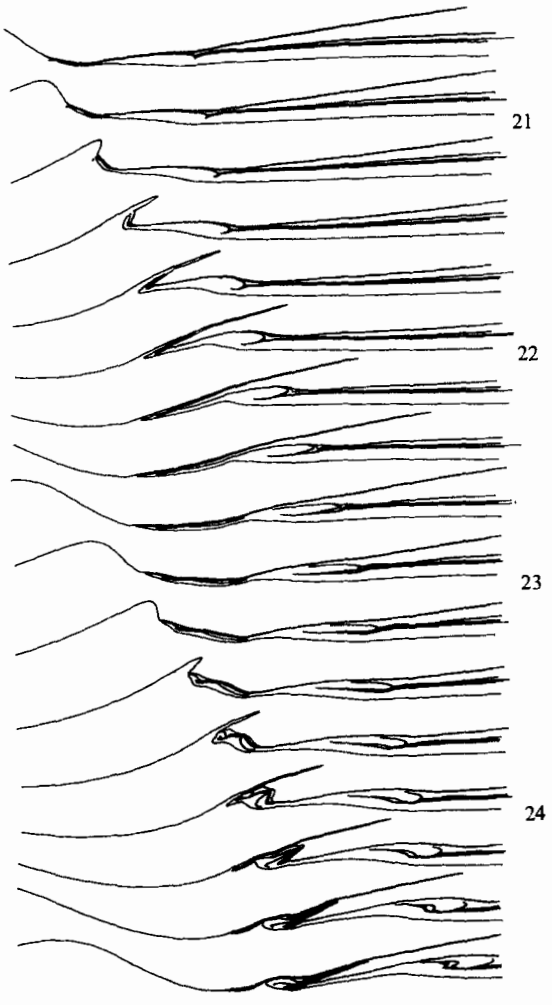

FIGURE 4. Same as in figure 3 but later in the evolution, between $t = 20.75$ and 24.75. Filaments are now being generated from multiple centres along the interface. The undulating interface ahead of the filamentation region causes parts of the filaments to develop forked structures by the action of oscillatory strain and shear. At this stage in the evolution, over 3600 nodes are being used to resolve the contour while the calculation began with 750 nodes. Excessively thin vorticity features are being removed by surgery at a scale 50 times smaller than the plotted line width.

Next, consider variations of the disturbance extent θ_0 and amplitude a in such a way that the product $am = 1$. Such a variation simply shrinks or expands the disturbance while preserving its shape. t_f versus $1/m$ is shown in figure 9 for both symmetric and antisymmetric initial conditions in planar geometry. t_f grows rapidly with $1/m$, possibly indicating that sufficiently broad disturbances will never commence filamentation. But, as $1/m \to 0$, t_f tends to become independent of the disturbance extent.

Finally, consider variations of the sphericity z_0 with $a = 0.025$ and $m = 40$. Figure 10 shows that t_f decreases with z_0^2 – filamentation occurs most readily in planar geometry.

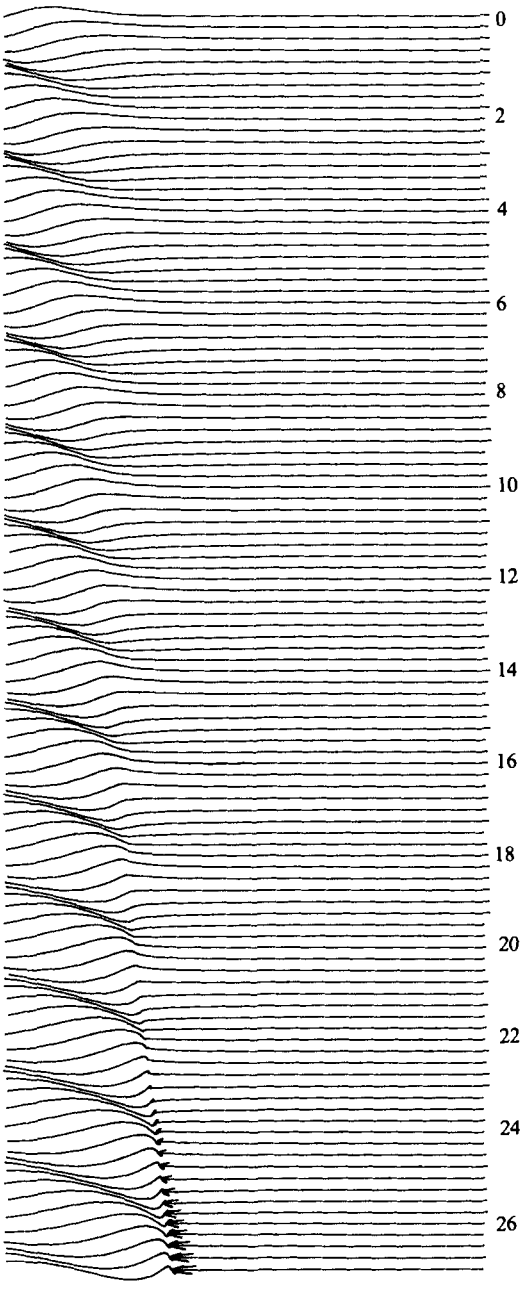

FIGURE 5. Filamentation of an initially antisymmetric disturbance to a vortex of hemispherical extent (case 19 of table 1).

4. Weakly nonlinear theory for circular vortices

By way of a mathematical analysis valid for shallow undular disturbances, the numerical results of the previous section, before the onset of filamentation, are extended in this section to include disturbances of arbitrarily small initial steepness. It is through this analysis that we can determine that almost all initial disturbances eventually commence filamentation.

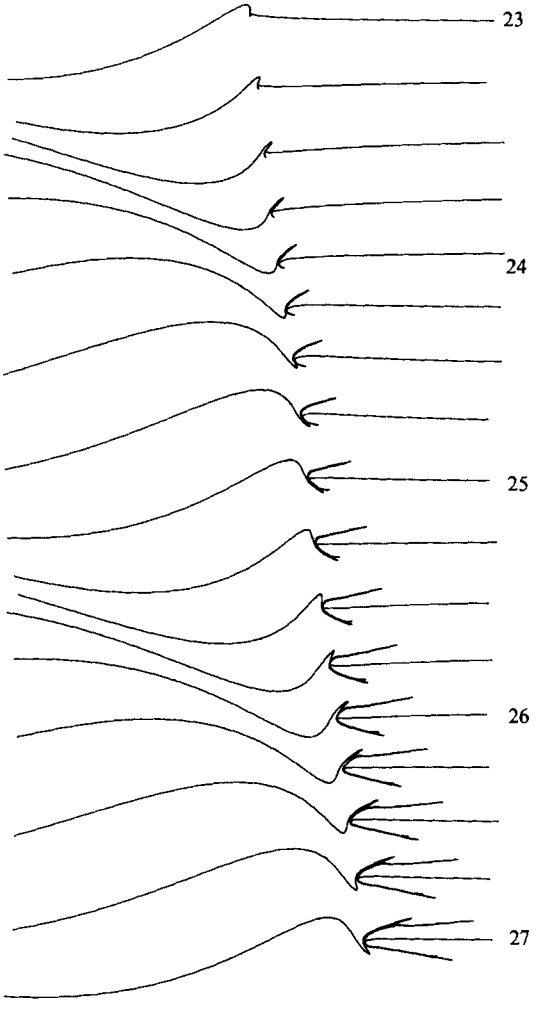

FIGURE 6. A close-up of figure 4 between $t = 23$ and 27.

The essential fact that makes the mathematical analysis possible is that, in a rotating frame that brings particles to rest along the equilibrium vortex boundary ($\Omega = \frac{1}{2}\omega$), linear disturbances proportional to $\exp(im\theta + i\sigma t)$, $m > 0$, have identical frequencies, $\sigma = \frac{1}{2}\omega$, both on the plane and on the sphere. This implies that a general initial disturbance of the form

$$\rho(\theta, 0) = \rho_0 + \sum_{m=1}^{\infty} \rho_m \, e^{im\theta} + \text{c.c.} \tag{3}$$

evolves periodically, in linear theory, according to

$$\rho(\theta, t) = \rho_0 + e^{\frac{1}{2}i\omega t} \sum_{m=1}^{\infty} \rho_m \, e^{im\theta} + \text{c.c.}, \tag{4}$$

where c.c. denotes complex conjugation and ρ_0 is a constant equal to the average value of ρ.

The weakly nonlinear equations are derived by using (4), but with time-dependent

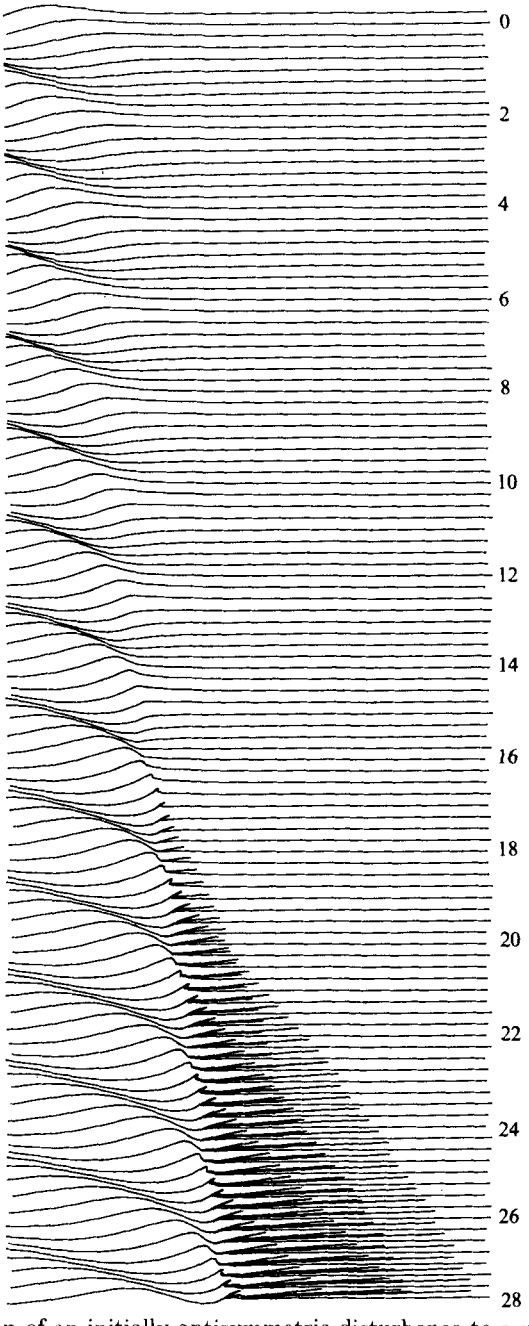

FIGURE 7. Filamentation of an initially antisymmetric disturbance to a vortex at a latitude of 45° north (case 20 of table 1).

coefficients $\rho_m(t)$, and by assuming both $\rho(\theta,t)$ and $\partial\rho(\theta,t)/\partial\theta$ are $O(a) \ll 1$. If one puts

$$\left.\begin{aligned} \rho(\theta,t) &= a[\bar{\eta}+\eta(\theta,t)], \quad \bar{\eta} = \frac{\rho_0}{a}, \\ \eta(\theta,t) &= A(\theta,t)\,\mathrm{e}^{\frac{1}{2}\mathrm{i}\omega t} + \text{c.c.}, \quad A(\theta,t) = \sum_{m=1}^{\infty} a_m(t)\,\mathrm{e}^{\mathrm{i}m\theta} \end{aligned}\right\} \tag{5}$$

Case	Fig. no.	Sym	z_0	m	a	Δ/a	t_f	ϵ_C (degrees)	t_m	μ	δ
1	—	S	1	60	1/60	0	17.7	1.27×10^{-5}	22.25	0.010	1×10^{-5}
2	—	S	1	40	1/40	0	19.7	3.50×10^{-4}	31.75	0.012	1×10^{-5}
3	—	S	1	30	1/30	0	21.5	1.14×10^{-3}	30.00	0.013	1×10^{-5}
4	—	S	1	20	1/20	0	25.5	4.76×10^{-3}	28.50	0.015	1×10^{-5}
5	—	S	1	10	1/10	0	43.7	4.78×10^{-3}	47.75	0.020	2×10^{-5}
6	—	S	0	40	$\sqrt{2}/40$	0	17.7	5.33×10^{-3}	29.00	0.015	2×10^{-5}
7	—	S	0	40	$(2/3)^{\frac{1}{2}}/40$	0	53.5	9.19×10^{-4}	53.50	0.010	1×10^{-5}
8	—	S	0	40	1/40	0	35.6	3.39×10^{-3}	45.00	0.012	1×10^{-5}
9	—	S	$\sqrt{2}/2$	40	1/40	0	27.4	3.11×10^{-2}	36.50	0.012	1×10^{-5}
10	—	S	1	40	1/40	0	21.2	3.66×10^{-4}	32.50	0.012	1×10^{-5}
11	—	S	1	40	1/80	0	95.7	1.04×10^{-3}	96.00	0.008	1×10^{-5}
12	—	A	1	60	1/60	0	12.6	2.09×10^{-5}	19.00	0.010	1×10^{-5}
13	2–4	A	1	40	1/40	0	12.6	9.29×10^{-5}	24.80	0.009	1×10^{-5}
14	—	A	1	30	1/30	0	12.7	1.44×10^{-4}	22.00	0.013	1×10^{-5}
15	—	A	1	20	1/20	0	14.7	4.82×10^{-4}	23.25	0.015	1×10^{-5}
16	—	A	1	10	1/10	0	20.9	8.19×10^{-3}	28.00	0.020	2×10^{-5}
17	—	A	0	40	$\sqrt{2}/40$	0	11.8	2.49×10^{-3}	23.50	0.015	2×10^{-5}
18	—	A	0	40	$(2/3)^{\frac{1}{2}}/40$	0	33.3	1.35×10^{-4}	33.50	0.010	1×10^{-5}
19	5, 6	A	0	40	1/40	0	20.9	1.85×10^{-3}	27.25	0.012	1×10^{-5}
20	7	A	$\sqrt{2}/2$	40	1/40	0	16.9	1.55×10^{-2}	28.00	0.012	1×10^{-5}
21	—	A	1	40	1/40	0	12.6	9.02×10^{-5}	22.50	0.012	1×10^{-5}
22	17	S	1	20	$\sqrt{2}/20$	0	13.2	1.41×10^{-2}	27.75	0.020	2×10^{-5}
23	20	S	1	20	$\sqrt{2}/20$	1/64	13.5, 14.0	1.19×10^{-2}	20.00	0.020	2×10^{-5}
24	19, 21	S	1	20	$\sqrt{2}/20$	1/32	14.1, 15.6	1.67×10^{-2}	20.00	0.020	2×10^{-5}
25	18	S	1	20	$\sqrt{2}/20$	1/16	17.4, 19.5	2.25×10^{-2}	23.75	0.020	2×10^{-5}
26	—	S	1	20	$\sqrt{2}/20$	1/8	22.0, 28.3	3.43×10^{-2}	28.50	0.020	2×10^{-5}
27	—	S	1	20	$\sqrt{2}/20$	1/4	>30	3.19×10^{-2}	29.75	0.020	2×10^{-5}
28	—	S	1	60	1/80	0	17.0	1.93×10^{-2}	29.40	0.015	1×10^{-5}
29	—	S	1	∞	0	0	15.3	7.68×10^{-4}	18.25	0.015	2×10^{-5}
30	—	A	1	∞	0	0	10.5	2.99×10^{-3}	15.00	0.015	2×10^{-5}

TABLE 1. Various parameters and diagnostics for the numerical calculations discussed in this paper. 'Sym' denotes symmetry, S being symmetric and A antisymmetric, z_0 is the sphericity, m and a together specify the size and shape of the disturbance, Δ is the interface width (used only in cases 23–27), t_f is the filamentation time (the two entries for cases 23–27 correspond to t_f on the upper and lower contours), ϵ_C gives one measure of accuracy though the accumulation of phase error (in degrees) by the end of the calculation $t = t_m$, and μ and δ are algorithm parameters described in §2. Cases 10 and 21 use the modified initial condition $r(\theta,0) = [1+2\rho(\theta,0)]^{\frac{1}{2}}$ to correspond to the spherical calculations of cases 8, 9, 19 and 20 (see Appendix A). Case 28 is an elliptical vortex calculation in which the initial condition is generated by first perturbing a circular vortex and then radially distorting the boundary to a nearly elliptical shape (it would be precisely elliptical if the originally circular vortex were not perturbed). Cases 29 and 30 are described in Appendix C.

into the fully nonlinear equations (see Appendix A) truncated at $O(a^4)$, one obtains

$$\left.\begin{aligned} &\frac{1}{\omega}\frac{\partial\eta(\theta,t)}{\partial t} - \frac{1}{4\pi}\int_0^{2\pi} \mathrm{d}\alpha \frac{\eta(\alpha,t)\sin(\alpha-\theta)}{1-\cos(\alpha-\theta)} = \frac{\partial G}{\partial\theta}, \\ &G(\theta,t) = \frac{a}{4}z_0\eta^2 - \frac{a^2}{4}(z_0^2+1)\,\bar{\eta}\eta^2 - \frac{a^2}{6}(z_0^2+1)\,\eta^3 - \frac{a^2}{24\pi}\int_0^{2\pi}\mathrm{d}\alpha\frac{[\eta(\alpha,t)-\eta(\theta,t)]^3}{1-\cos(\alpha-\theta)}, \end{aligned}\right\} \quad (6)$$

where the function G contains all the nonlinearity up to cubic order (the planar result, obtained by putting $z_0 = 1$, and by replacing η by $\eta+\frac{1}{2}\eta^2$, is actually more

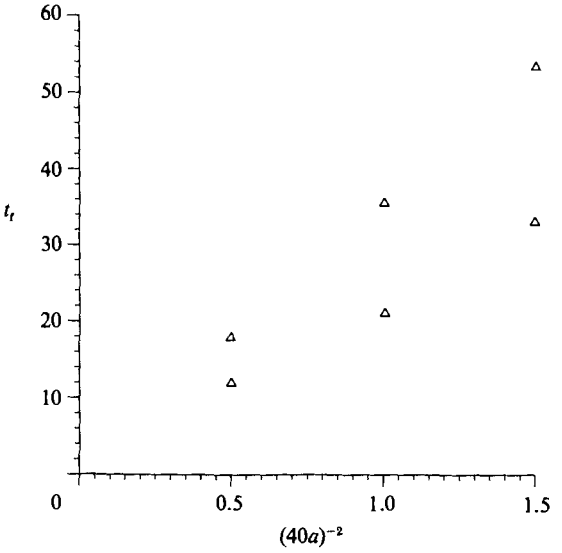

FIGURE 8. The variation of the filamentation time t_f with the inverse-squared amplitude of the disturbance for fixed extent $\theta_0 = \pi/40$ and sphericity $z_0 = 0$ (equatorial vortices). Data for both symmetric (upper triangles) and antisymmetric (lower triangles) initial conditions are shown.

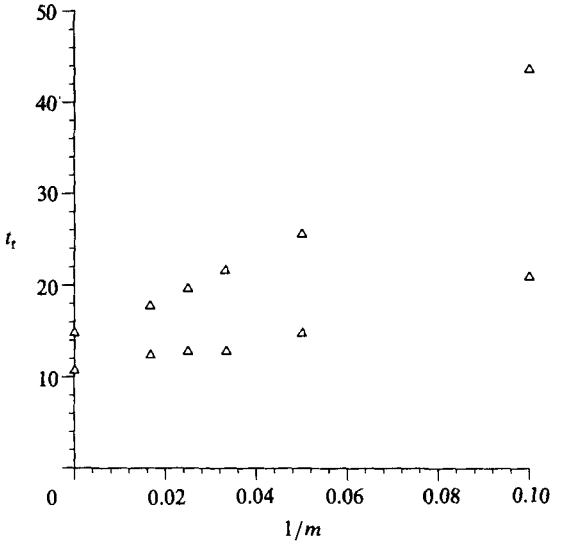

FIGURE 9. t_f versus disturbance size (measured by $1/m$) for planar vortices. Data for both symmetric (upper triangles) and antisymmetric (lower triangles) initial conditions are shown. (The calculations with $1/m = 0$, cases 29 and 30 of table 1, were performed with a periodic version of the planar contour-surgery algorithm discussed in Appendix C.)

difficult to derive than the above spherical result!). Using (5), one finds that the left-hand side of (6) is simply

$$\frac{1}{\omega}\frac{\partial A(\theta,t)}{\partial t}\,\mathrm{e}^{\frac{1}{2}\mathrm{i}\omega t} + \text{c.c.}, \tag{7}$$

but the function $G(\theta,t) \ll 1$; therefore, A must depend on at least two timescales, t and, as shown in Appendix A, a^2t – *not at*. The quadratic nonlinearity, $\frac{1}{4}az_0\eta^2$, is not

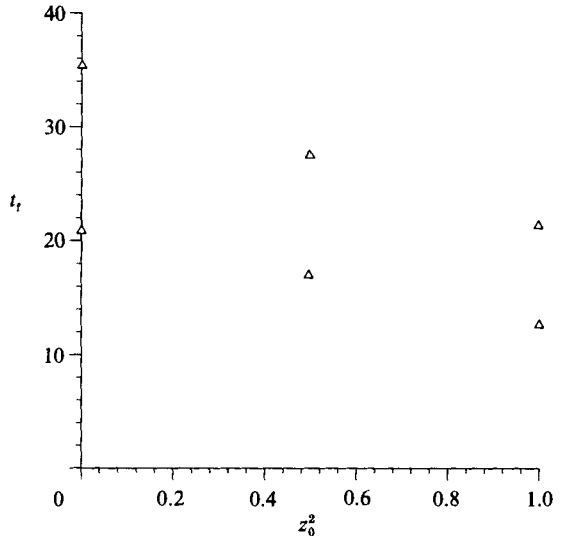

FIGURE 10. t_f versus z_0^2 for fixed disturbance amplitude $a = 1/40$ and extent $\theta_0 = \pi/40$. Data for both symmetric (upper triangles) and antisymmetric (lower triangles) initial conditions are shown. The calculations with $z_0 = 1$ were performed using the planar numerical algorithm but with the initial disturbance modified to $r(\theta, 0) = [1+2\rho(\theta, 0)]^{\frac{1}{2}}$ to ensure a proper correspondence to the spherical calculations (see Appendix A).

alone responsible for the evolution of the envelope A (indeed, this term is altogether absent for equatorial situations, $z_0 = 0$). Expanding $A(\theta, t)$ in the series

$$A(\theta, t) = A_0(\theta, \tau) + aA_1(\theta, t, \tau) + a^2 A_2(\theta, t, \tau) + \ldots, \tag{8}$$

with $\tau \equiv \omega a^2 t$, one finds that A_0 evolves according to

$$\left.\begin{aligned}
&\frac{\partial A_0(\theta,\tau)}{\partial \tau} = \frac{\partial B_0}{\partial \theta},\\
&B_0(\theta,\tau) = \tfrac{1}{2}\mathrm{i}z_0^2\left(A_0\frac{\partial}{\partial\theta}(W_0 - W_0^*) - |A_0|^2\frac{\partial A_0}{\partial\theta}\right) - \tfrac{1}{2}(z_0^2+1)\,|A_0|^2 A_0\\
&\qquad\qquad - \frac{1}{8\pi}\int_0^{2\pi} \mathrm{d}\alpha\,\frac{|A(\alpha,\tau)-A(\theta,\tau)|^2[A(\alpha,\tau)-A(\theta,\tau)]}{1-\cos(\alpha-\theta)},\\
&A_0(\theta,\tau) = \sum_{m=1}^{\infty} a_{0m}(\tau)\,\mathrm{e}^{\mathrm{i}m\theta},\\
&W_0(\theta,\tau) = \sum_{m=1}^{\infty} w_{0m}(\tau)\,\mathrm{e}^{\mathrm{i}m\theta},\\
&|A_0|^2 = W_0 + W_0^* + \sum_{m=1}^{\infty} |a_{0m}|^2,
\end{aligned}\right\} \tag{9}$$

the last equation defining W_0 (* denotes complex conjugation). In the first equation, only the part of B_0 that can be expressed as $\sum_{m=1}^{\infty} b_{0m}(\tau)\,\mathrm{e}^{\mathrm{i}m\theta}$ is intended. Knowledge of A_0 allows one to compute higher-order terms explicitly; for example, A_1 is given by

$$A_1(\theta, t, \tau) = \mathrm{i}z_0\frac{\partial}{\partial\theta}(W_0\,\mathrm{e}^{-\frac{1}{2}\mathrm{i}\omega t} - \tfrac{1}{2}A_0^2\,\mathrm{e}^{\frac{1}{2}\mathrm{i}\omega t}). \tag{10}$$

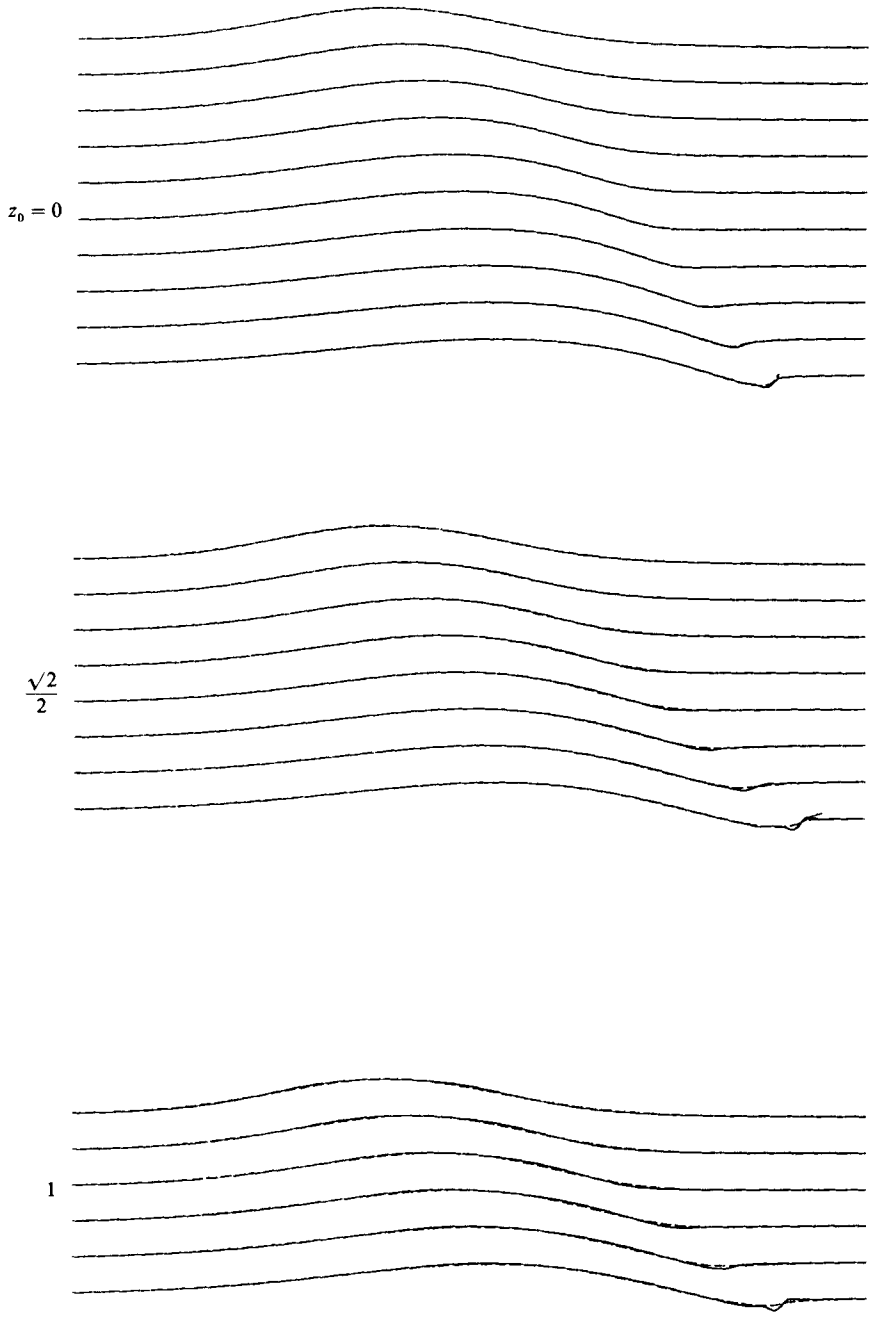

FIGURE 11. A comparison between the weakly nonlinear theory (solid lines) and the fully nonlinear theory (dashed lines) for initially symmetric disturbances for three latitudes: equatorial ($z_0 = 0$), mid-latitudes ($z_0 = \sqrt{2}/2$), and polar ($z_0 = 1$). Time proceeds downwards in the three cases with successive curves drawn two disturbance periods ($\Delta t = 4$) apart. Note that steepening always occurs on the right whereas the opposite occurs on the left.

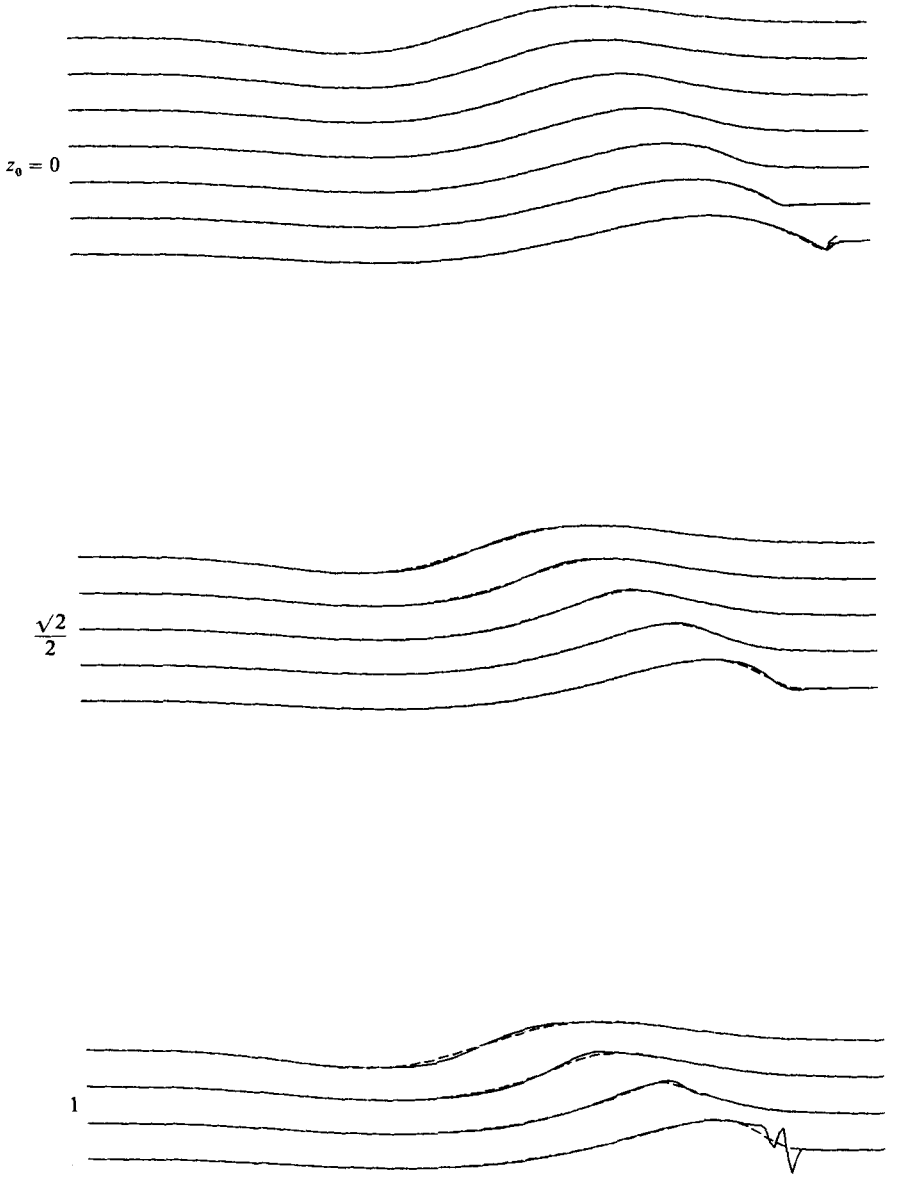

FIGURE 12. Same as in figure 11 but for antisymmetric initial disturbances.

Equations (9) and (10) admittedly look more complicated than the original fully nonlinear equations, but the essential property of (9) is that the right-hand side is precisely cubic in A_0. This implies that (9) is unchanged if A_0 is replaced by cA_0 and τ by τ/c^2, where c is a constant. That is, if the amplitude is halved, the evolution proceeds four times more slowly, but the form of the evolution is identical.

With this observation in mind, consider comparing some of the fully nonlinear calculations in table 1 with the weakly nonlinear theory (keeping only A_0 and A_1 in (9)). Appendix A describes the numerical computation and initialization of (8), and only the results of those computations are described here. Figures 11 and 12, the central results of this paper, compare the weakly nonlinear theory (solid lines) with

the fully nonlinear theory (dashed lines) every two disturbance periods for $z_0 = 0$, $\sqrt{2}/2$, and 1 for symmetric and antisymmetric initial conditions respectively ($a = 0.025$, $m = 40$). The poorer comparisons for larger z_0 are an artifact of initialization, which is impossible to perfect in the weakly nonlinear theory (see Appendix A). Nonetheless, given that the weakly nonlinear theory is valid only for small steepness ($\partial\rho(\theta, t)/\partial\theta \ll 1$), the comparisons are remarkable right up to the time at which filamentation commences. In each case, the numerical solution of the weakly nonlinear equation (8) breaks down just after filamentation commences in the corresponding fully nonlinear calculation. Thus the weakly nonlinear calculations not only closely agree with the fully nonlinear ones over the steepening stage, but also predict, by their own breakdown, the approximate time at which the vortex boundary commences filamentation.

Had we compared calculations for disturbances, say, half as steep as those in figures 11 and 12, we would have found an even closer correspondence. This is simply because the weakly nonlinear theory becomes a better approximation of the fully nonlinear theory. The weakly nonlinear calculations, however, need not be recomputed, for they are the same as shown in figures 11 and 12. Thus, if one could perform the fully nonlinear calculations in this case, one would observe filamentation once again, occurring after a time four times longer than found for the calculations in figures 11 and 12. Again, one could reduce the amplitude of the initial disturbance by another factor of two, still better correspondence between the weakly and fully nonlinear theories occurring in this case, and again filamentation would eventually commence, after a time four times longer still. Of course, there is no limit to this sequence: an arbitrarily shallow disturbance will eventually commence filamentation.

5. Filamentation of non-circular interfaces

Figure 13 illustrates the evolution of a small disturbance initially on the right-hand tip of an elliptical vortex (semimajor axis length = 1, semiminor axis length = $\frac{2}{3}$). No dramatic change in the gross shape of the vortex occurs, indeed the vortex is linearly stable at this aspect ratio (Love 1893), but a closer inspection of the boundary at a time slightly beyond the last frame (figure 14) reveals great complexity. Filamentation in fact commences at $t = t_f \approx 17$ and, compared with the circular vortex calculations of §3, leads to a more rapid distortion of the vortex boundary. The greater complexity of filamentation results from the additional effects of variable shear and strain, effects that, it is shown below, increase the rate of steepening of shallow disturbances relative to corresponding disturbances on circular vortices. The intuitive argument is given first and the mathematical one follows.

A very small, localized disturbance (a disturbance with maximum curvature greatly exceeding that of the supporting interface) travels around the ellipse as if it were a fluid particle on the equilibrium interface, except that it also undergoes a nearly periodic oscillation similar to that occurring on circular vortices. The difference from circular vortices is that the velocity field tangent to the ellipse is no longer uniform, giving rise to the additional effects of strain and variable shear. For example, as a disturbance moves from the position of the semimajor axis to the semiminor axis, the tangential velocity accelerates causing fluid particles along the equilibrium boundary to be pulled apart; fluid particles are then compressed on the approach to the semimajor axis. One can see an immediate (linear) effect on a disturbance: the disturbance stretches while travelling from the semimajor to the

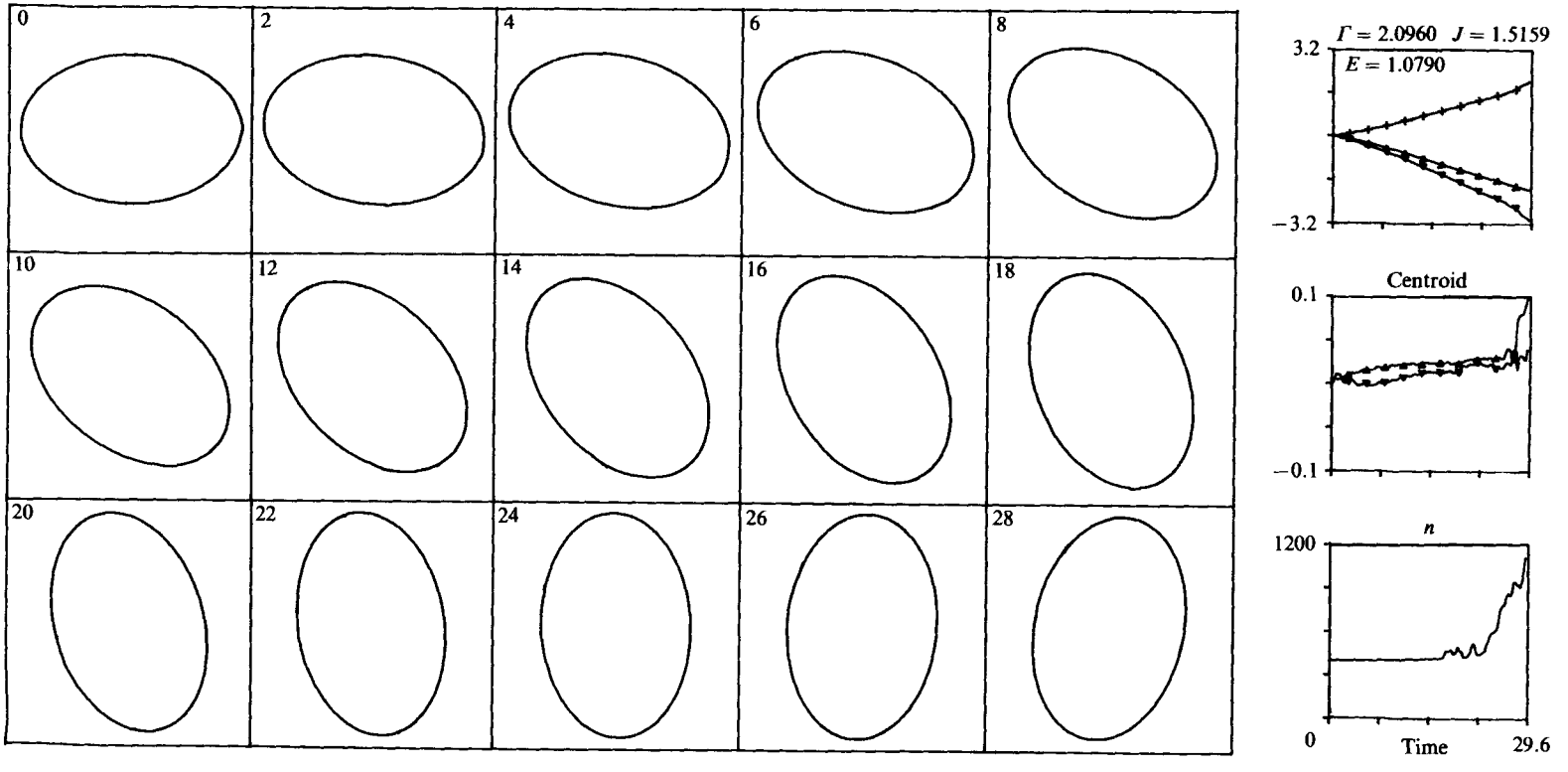

FIGURE 13. The evolution of an elliptical vortex perturbed initially by a symmetric disturbance on the vortex's right tip (case 28 of table 1). Time is indicated in the upper left-hand corner of each frame. The vortex makes nearly half a revolution per frame during which time the disturbance, hardly recognizable in this plot, travels almost a complete circuit of the boundary. The panels on the right give an indication of the accuracy of the calculation. The upper panel displays, as a function of time, departures of circulation Γ ($\triangle$), angular momentum J (∇), and energy E ($+$) from exact conservation *multiplied by* 10^4. The middle panel displays the errors in x centroid x_c ($\triangle$) and y centroid y_c (∇) similarly multiplied by 10^4. The bottom panel shows the total number of nodes.

FIGURE 14. A greatly enlarged view of a small part of the elliptical boundary at $t = 29.35$ (the interior of the vortex is on the left).

semiminor axis and compresses (steepens) on the journey from the semiminor to the semimajor axis. The nonlinear effect is to more quickly steepen the disturbance during the periods of compression than during the equal periods of extension. A net gain in steepening is thereby registered over the steepening that would be experienced by a disturbance of the same form on a circular vortex.

The qualitative arguments above may be justified by the mathematical analysis of Appendix B from which only the central results are taken. These include two. The first proves that infinitely localized disturbances (defined below) obey fully nonlinear equations for the evolution of a disturbance to an infinitely straight contour in the presence of time-varying strain and shear. The second shows that a universal equation, dependent only on the shape of the initial disturbance and some integral measure of strain and shear, governs the steepening of shallow disturbances under very general circumstances.

Under the conditions that the amplitude and extent of a disturbance be

exceptionally smaller than any lengthscale in the supporting (piecewise-constant) flow, that is, less than the minimum radius of curvature of the interface along which the disturbance propagates and less than the distance between interfaces if there are more than one, and under the single further condition that the curvature of the disturbance (the ratio of its amplitude to its extent squared) greatly exceeds the curvature of the supporting interface, the disturbance, in a right-handed coordinate system moving along the supporting interface (as illustrated in figure 15), satisfies

$$\left.\begin{aligned} \dot{\xi} &= \frac{\omega}{4\pi}\int_{C_\infty} \{\log[(\xi-\xi')^2+(\eta-\eta')^2]-\log[\xi-\xi']^2\}\,\mathrm{d}\xi'+\gamma\xi+\alpha\eta, \\ \dot{\eta} &= \frac{\omega}{4\pi}\int_{C_\infty} \log[(\xi-\xi')^2+(\eta-\eta')^2]\,\mathrm{d}\eta'-\gamma\eta. \end{aligned}\right\} \tag{11}$$

Here, the disturbance has been scaled by its (infinitely) small extent, C_∞ is an infinitely long curve (the vorticity interface in these scaled coordinates) for which $\eta\to 0$ as $|\xi|\to\infty$, $\gamma(t)$ is the strain parallel to the interface at the position of the disturbance, and $\alpha(t)$ is the shear. α is equal to twice the rotation rate of the coordinate axes minus the average of the vorticity just inside and outside the interface. γ and α depend only on the (basic state) velocity gradients along the supporting interface – they are independent of the disturbance – and for steady supporting flows (e.g. a rotating ellipse, see Appendix B for details), γ and α are periodic functions of time, with a period equal to the time a particle takes to circuit the interface. Note that (11) predicts the same form of evolution for a given disturbance shape of arbitrary scale.

The restriction to infinitely localized disturbances is essential to the derivation of (11) and renders it amenable to a weakly nonlinear, two-timescales analysis. Without the assumption of infinite localization, disturbances to variable-curvature interfaces do not have equal frequencies in any reference frame, and it is this equal-frequency requirement that is vital to the weakly nonlinear theory. Of course, the straight supporting interface in (11) does support equal-frequency linear waves, $\exp[\mathrm{i}(k\xi-\frac{1}{2}\omega t)]$, $k>0$, and an analysis similar to that described in §4 and Appendix A for circular vortices (see Appendix B) produces

$$\left.\begin{aligned} \eta(\xi,t) &= \epsilon[\bar{\eta}+\tilde{\eta}(\xi,t)], \quad \epsilon\ll 1, \\ \tilde{\eta}(\xi,t) &= A(\xi,t)\,\mathrm{e}^{\frac{1}{2}\mathrm{i}\omega t}+\text{c.c.}, \\ A(\xi,t) &= \int_0^\infty \mathrm{d}k F(k)\,\mathrm{e}^{-\mathrm{i}k\xi} \\ &= A_0(\xi,\tau)+\epsilon A_1(\xi,t,\tau)+\epsilon^2 A_2(\xi,t,\tau)+\ldots, \\ \tau &= \omega\epsilon^2 t, \\ \frac{\partial A_0(\xi,t)}{\partial\tau} &= \langle\beta^2\rangle\frac{\partial B_0}{\partial\xi}, \\ B_0(\xi,t) &= \tfrac{1}{2}\mathrm{i}\sigma\left(A_0\frac{\partial}{\partial\xi}(W_0-W_0^*)-|A_0|^2\frac{\partial A_0}{\partial\xi}\right) \\ &\quad +\frac{1}{4\pi}\int_{-\infty}^{\infty}\mathrm{d}\xi'\frac{|A_0(\xi',\tau)-A_0(\xi,\tau)|^2[A_0(\xi',\tau)-A_0(\xi,\tau)]}{(\xi'-\xi)^2}, \end{aligned}\right\} \tag{12}$$

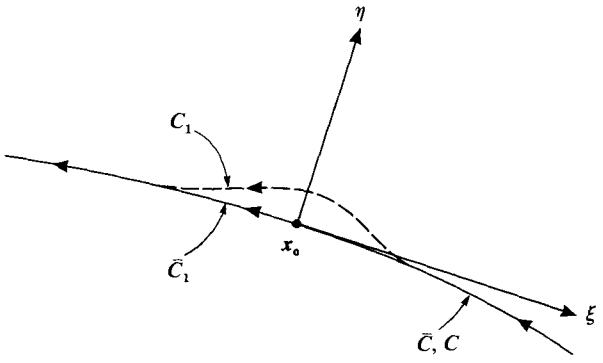

FIGURE 15. The local coordinate system defined by the motion of the fluid particle $x_0(t)$ along the supporting interface.

where, as in the circular case, W_0 is one-half of the spectrum of $|A_0|^2$, only one-half of the spectrum of B_0 is intended, * denotes complex conjugation, and the constants $\langle\beta^2\rangle$ and σ are integral measures of the strain and shear (see Appendix B). $\langle\beta^2\rangle$ may be absorbed into the definition of the long timescale τ, in which case the envelope equation for A_0 is seen to depend only on the shape of the disturbance and the constant σ.

This simple structure of the envelope equation has important implications for the evolution of shallow localized disturbances. In the previous section, close agreement was demonstrated between the fully and weakly nonlinear calculations (figures 11 and 12) for circular vortices. And from this correspondence and the mathematical structure of the weakly nonlinear equations, we concluded that arbitrarily shallow disturbances eventually commence filamentation. The same conclusion, it is argued, applies to the evolution of infinitely localized disturbances under very general circumstances. First, the weakly nonlinear equation (12) is simply the limiting form of the corresponding equation for circular vortices (9), for σ between 0 and 1. Second, the data presented in figure 9 show that localized disturbances commence filamentation sooner than less localized ones, all other things being equal. Third, the data of figure 10, with σ identified with z_0^2, suggest that the filamentation time would continue to decrease if σ was taken to values greater than 1. These facts combined with the observed close agreement between the fully and weakly nonlinear calculations in figures 11 and 12 support the view that filamentation eventually occurs for almost all initial disturbances of any steepness whatever.

6. Filamentation of finite gradients of vorticity

In this section, a series of numerical calculations is used to examine the evolution of shallow disturbances to sharp but not infinitely sharp vorticity gradients. It is found that disturbances with amplitudes greatly exceeding the effective width of the interface evolve in much the same way as they would on an interface of zero width. Filamentation is not simply an artifact of the questionable assumption of piecewise-constant vorticity. However, profound differences are seen to occur when the disturbance amplitude is comparable with (but still a factor of ten larger than) the interface width.

To demonstrate these effects, a finite gradient of vorticity is approximated by replacing a single circular contour (on the plane) by two contours separated initially

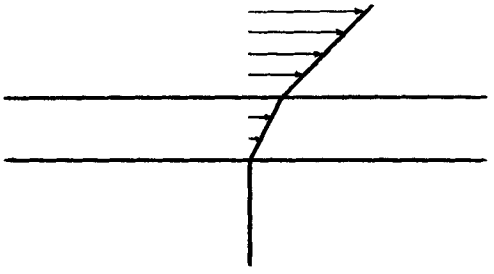

FIGURE 16. Two interfaces across each of which the vorticity jumps by $\frac{1}{2}\omega$ and the associated velocity field.

by a width Δ. The use of two contours can be justified, so long as the interface width remains much smaller than the radius of curvature of the mean interface position, by noting that the linear long-wave dispersion relation has a form common to all profiles of vorticity across the interface. For example, in the simpler but relevant problem of two straight interfaces, across each of which the vorticity jumps by $\frac{1}{2}\omega$ (see figure 16), one eigenmode is sinuous and the other varicose. The sinuous one describes the motion of the mean interface position, and a disturbance of the form $\exp[\mathrm{i}(kx-\sigma t)]$ has the following dispersion relation for wavelengths long compared with the interface width Δ:

$$\sigma = \tfrac{1}{2}\omega[1+\tfrac{1}{2}(k\Delta)^2], \tag{13}$$

clearly indicating the dispersive nature of two interfaces. The key point is that the *same* long-wave dispersion relation holds for general profiles of vorticity, only the constant multiplying $(k\Delta)^2$ depends on the profile.

The calculations are initialized as follows. After adding, a symmetric disturbance ($a = \sqrt{2}/20$, $m = 20$) to a unit circular vortex, the resultant boundary is divided into two by multiplying it by $1+\frac{1}{2}\Delta$ and $1-\frac{1}{2}\Delta$. The case with $\Delta = 0$ or no interfacial width is given in figure 17. By $t = t_{\mathrm{f}} \approx 13.2$, filamentation commences, and proceeds with growing complexity as observed previously (e.g. figure 2). Figures 18, 19 and 20 show calculations with three successively smaller values of Δ: $a/16$, $a/32$ and $a/64$. The new phenomenon illustrated in all three figures is the formation of a pocket of intermediate-vorticity fluid between the two contours; see figure 21 for a close-up of figure 19). The pocket forms by the nonlinear pumping, by the undulating disturbance, of fluid from the stretching interface to the left of the pocket. The stretching is accomplished by the variation of strain induced by the disturbance along different parts of the interface; compression near the pocket brings fluid into it. The secular effect of this action is to swell the pocket until the mean shear can succeed in tilting part of the disturbance over. The filamentation of a single interface occurs for precisely analogous reasons, except that the pocket is infinitely thin.

Figures 18–20 demonstrate convergence to the single-interface calculation of figure 17. Not only does the pocket get smaller with decreasing interface width, but the two interfaces begin to commence filamentation together. On the other hand, widening the interface, say to twice the width shown in figure 18, further delays filamentation and gives rise to an extended pocket region upon which varicose disturbances can be seen to propagate away from the left-hand position of the pocket (not shown). Upon widening the interface by another factor of two ($\Delta = a/4$), no filamentation is seen to take place up to $t = 30$ although some steepening is observed (not shown). The

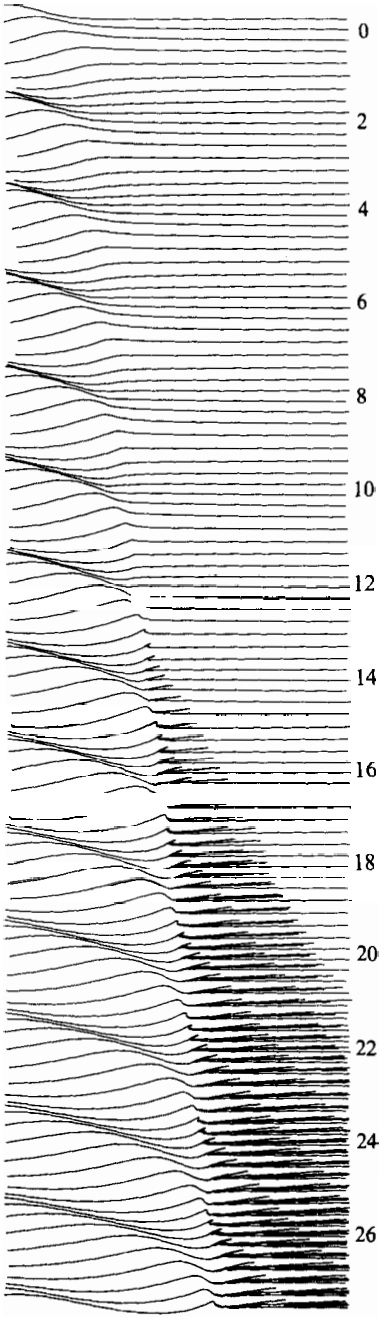

Fig. 17

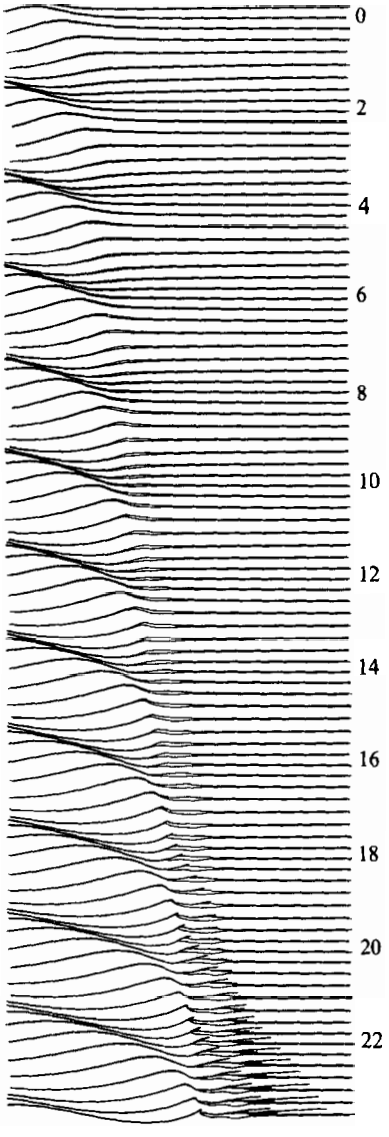

Fig. 18

FIGURE 17. Filamentation in the limit of zero interface width (a single contour). This figure should be compared with figures 18–20 in which the interface widths are finite (case 22 of table 1).
FIGURE 18. As in figure 17 but for an interface width $\Delta = a/16$ (case 25).

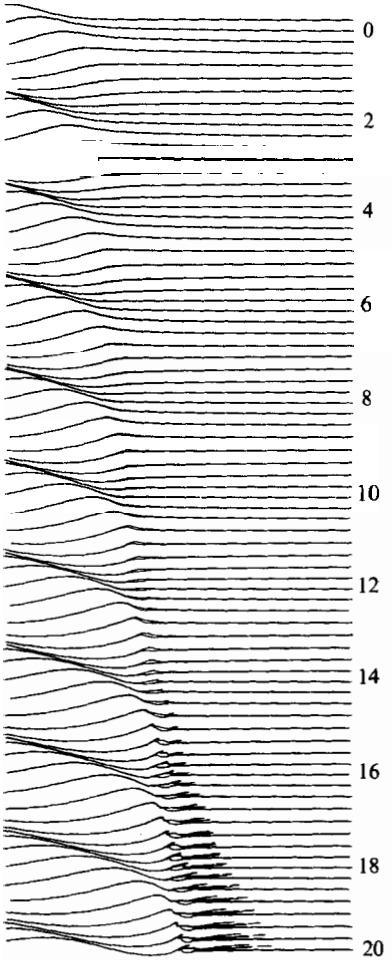

Fig. 19

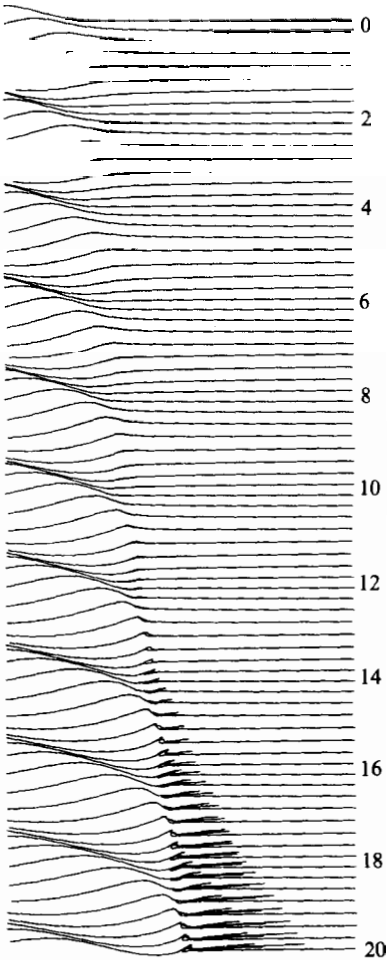

Fig. 20

FIGURE 19. As in figure 18 but with half the interface width $\Delta = a/32$ (case 24).
FIGURE 20. As in figure 19 but with half again the interface width $\Delta = a/64$ (case 23).

numerical results are summarized in figure 22 with a graph of the filamentation time on either interface versus the interface width/amplitude ratio.

Finite gradients of vorticity are thus seen to dramatically affect filamentation. The details of filamentation, e.g. the nature of the pocket, almost certainly depend on the profile of vorticity assumed, but the most important effect of a finite interface is to retard filamentation for amplitudes comparable with the interface width. However, filamentation, in the sense that vorticity contours eventually buckle, probably occurs even for these amplitudes. Indeed, in the extreme case opposite to an infinitely sharp interface, that of arbitrarily shallow disturbances to a flow with a *uniform* vorticity gradient, the vorticity contours still buckle (see, for example, figure 1 of Haynes 1987).

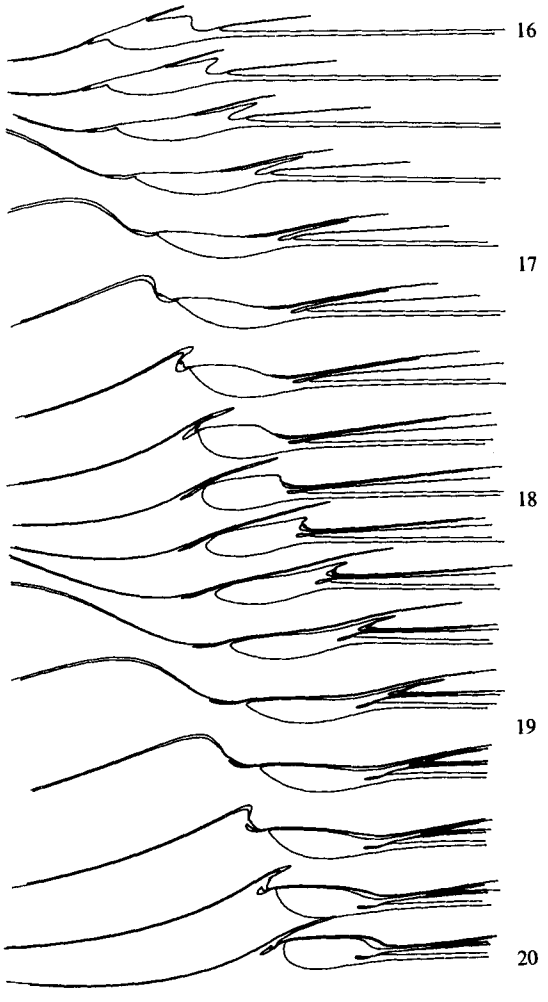

FIGURE 21. An enlarged view of the interface in the intermediate case (figure 19) between $t = 16$ and 20.

7. Discussion

Filamentation may be regarded as one particularly interesting case of a more generally defined phenomenon, that of Rossby-wave breaking (McIntyre & Palmer 1983, 1984, 1985). Rossby-wave breaking encompasses any unsteady motion characterized by the irrevocable deformation of vorticity contours (in an inviscid, incompressible fluid). Filamentation, by contrast, is the eventual qualitative change in the behaviour experienced by small, shallow disturbances to sharp interfaces of vorticity, disturbances that had been thought to remain undular forever (Stern 1985; Stern & Pratt 1985).

On the basis of the calculations in the previous section, in which a finite interface was seen to dramatically retard filamentation (cf. figure 22), it is hypothesized that filamentation acts to suppress itself by widening the interface through the nonlinear mixing of vorticity across the interface. The mixing is not assumed to be perfect, rather, a band of sheared two-dimensional turbulence is envisaged whose width is of the same order as the amplitude of the initial disturbance.

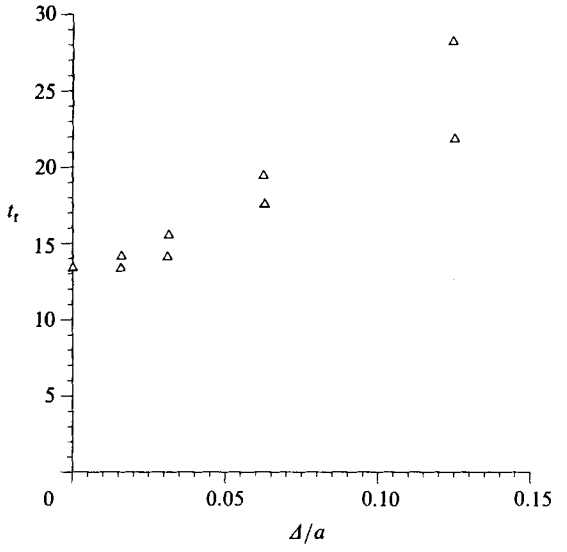

FIGURE 22. A summary of the finite interface calculations. The filamentation time t_f is plotted versus Δ/a for both the upper and the lower contours.

The results of this paper do not apply to disturbances whose extent or effective wavelength is comparable with the radius of curvature of the supporting interface. Indeed, in figure 9, the filamentation time was found to rise sharply with the extent of the initial disturbance, suggesting that either filamentation takes a very long time or else never occurs for disturbances sufficiently broad. It seems inconceivable, however, that an unsteady (aperiodic) flow can resist accessing more and more of the infinite spectral range of smaller scales. That is, nonlinear interactions in an unsteady flow seem likely to excite continually smaller scales until a scale is reached at which filamentation occurs.

Recent high-resolution spectral calculations of a one-layer model of the wintertime stratosphere (Juckes & McIntyre 1987) have illustrated the importance of nonlinear vortex dynamics in shaping the structure of an intense vortex situated close to the winter pole. The arrival of planetary-scale Rossby waves from the troposphere below subjects the vortex to a disturbance whose amplitude is much larger than those considered in this paper. The effect of the initial, larger-amplitude wave-breaking event is to sweep away the outermost (potential) vorticity contours of the initially broader vortex, thereby creating a narrow band of exceedingly high vorticity gradients. (A similar mechanism of gradient intensification operates for sufficiently eccentric elliptical distributions of vorticity in planar geometry – see Melander, McWilliams & Zabusky 1987 and Dritschel 1988*b*, figures 11 and 12). These extreme gradients of vorticity then become susceptible to filamentation. Small perturbations, perhaps arising from the inhomogeneities in the surrounding relatively weak vorticity field, inexorably steepen and commence filamentation. In summary, major nonlinear events, events that alter the large-scale structure of the flow, rapidly intensify vorticity gradients surrounding intense vortices while the more subtle nonlinear process of filamentation utilizes small, arbitrarily small, perturbations to diminish (in a coarse-grained sense) the vorticity gradients. In an episodically forced system like the stratosphere, or in turbulence, both processes operate simultaneously to produce exquisitely complicated behaviour.

I would especially like to thank M. E. McIntyre and N. J. Zabusky for their valuable comments during the development of this research and manuscript.

Appendix A. Weakly nonlinear theory for circular vortices

In this Appendix, shallow disturbances to circular vortices on the plane or the sphere are shown to satisfy a cubically nonlinear envelope equation evolving on a timescale inversely proportional to the initial amplitude of the disturbance squared. The essential characteristic of this equation is that its *form* of evolution is independent of the disturbance amplitude. The following derivation applies to the fully spherical case, the planar result being obtained as an appropriate limit noted below.

Suppose the equilibrium vortex lies at the axial position $z = z_0$, $-1 < z_0 < 1$. The disturbed vortex is most conveniently represented in the form

$$z(\theta, t) = z_0 - r_0^2 \rho(\theta, t), \tag{A 1}$$

where $r_0^2 = 1 - z_0^2$, for then the perturbation shifts the equilibrium colatitude by the approximate amount $r_0 \rho(\theta, t)$ and also because the relationship between ρ and the corresponding disturbance quantity on the plane in the limit $z_0 \to 1$ is simple.

Using the following parameterization for the contour:

$$\left.\begin{aligned} x = r\cos\theta, \quad y = r\sin\theta, \\ z = z_0 - r_0^2\rho, \quad r = (1-z^2)^{\frac{1}{2}}, \end{aligned}\right\} \tag{A 2}$$

the contour dynamical equations (1), in a frame of reference rotating at half the vorticity jump across the interface, may be rewritten as

$$\left.\begin{aligned} \frac{\mathrm{d}\rho(\theta,t)}{\mathrm{d}t} &= -\frac{\omega}{4\pi}\int_0^{2\pi} \mathrm{d}\alpha \log|\boldsymbol{x}(\alpha,t)-\boldsymbol{x}(\theta,t)|^2 \frac{\partial\rho(\alpha,t)}{\partial\alpha}, \\ r(\theta,t)\frac{\mathrm{d}\theta}{\mathrm{d}t} &= -\tfrac{1}{2}\omega r(\theta,t) - \frac{\omega}{4\pi}\int_0^{2\pi} \mathrm{d}\alpha \log|\boldsymbol{x}(\alpha,t)-\boldsymbol{x}(\theta,t)|^2 \frac{\partial}{\partial\alpha}[r(\alpha,t)\sin(\alpha-\theta)]. \end{aligned}\right\} \tag{A 3}$$

The immediate task is to simplify these equations under the condition that both ρ and $\partial\rho/\partial\theta$ are small compared with unity. Only terms up to third order are required, and for this it is necessary to expand r and $\log|\boldsymbol{x}(\alpha,t)-\boldsymbol{x}(\theta,t)|^2$ to only second order (here the planar derivation is more difficult, since third-order terms would be required). These expansions take the form

$$\left.\begin{aligned} r &= r_0(1+2z_0\rho-r_0^2\rho^2)^{\frac{1}{2}} \\ &\approx r_0(1+z_0\rho-\tfrac{1}{2}\rho^2), \\ \log|\boldsymbol{x}(\alpha,t)-\boldsymbol{x}(\theta,t)|^2 &\approx \text{constant} + \log[1-\cos(\alpha-\theta)] + z_0\rho(\alpha,t) \\ &\quad -\rho(\theta,t)\rho(\alpha,t) - \tfrac{1}{2}z_0^2\rho^2(\alpha,t) + \frac{\cos(\alpha-\theta)[\rho(\alpha,t)-\rho(\theta,t)]^2}{2[1-\cos(\alpha-\theta)]}, \end{aligned}\right\} \tag{A 4}$$

where the constant depends on θ and t but not α and so contributes nothing to the integrals in (A 3).

In the planar case, the natural definition of the perturbation is $r/r_0 = 1+\tilde{\rho}$. One may therefore obtain the planar results by putting $z_0 = 1$ and replacing ρ by

$\tilde{\rho}+\frac{1}{2}\tilde{\rho}^2$ throughout (equivalently, of course, one can repeat this exercise starting from planar contour dynamics, but the task is more arduous and the result less pleasing!).

The expressions for $\mathrm{d}\rho/\mathrm{d}t$ and $\mathrm{d}\theta/\mathrm{d}t$ follow after considerable yet straightforward algebraic manipulations, whence from

$$\frac{\partial\rho}{\partial t}+\frac{\mathrm{d}\theta}{\mathrm{d}t}\frac{\partial\rho}{\partial\theta}=\frac{\mathrm{d}\rho}{\mathrm{d}t}, \tag{A 5}$$

and upon substituting the expression

$$\rho(\theta,t)=a[\bar{\eta}+\eta(\theta,t)], \quad a\ll 1 \tag{A 6}$$

one obtains (6) rewritten here for clarity:

$$\left.\begin{aligned}&\frac{1}{\omega}\frac{\partial\eta(\theta,t)}{\partial t}-\frac{1}{4\pi}\int_0^{2\pi}\mathrm{d}\alpha\,\frac{\eta(\alpha,t)\sin(\alpha-\theta)}{1-\cos(\alpha-\theta)}=\frac{\partial G}{\partial\theta},\\ &G(\theta,t)=\frac{a}{4}z_0\eta^2-\frac{a^2}{4}(z_0^2+1)\bar{\eta}\eta^2-\frac{a^2}{6}(z_0^2+1)\eta^3-\frac{a^2}{24\pi}\int_0^{2\pi}\mathrm{d}\alpha\,\frac{[\eta(\alpha,t)-\eta(\theta,t)]^3}{1-\cos(\alpha-\theta)}.\end{aligned}\right\} \tag{A 7}$$

Since the nonlinear function G is $O(a)\ll 1$, the solution to (A 7) depends on at least two timescales. One might expect a dependence on the long timescale at, but the periodicity of the lowest-order solution necessitates the choice a^2t. Defining then $\tau=\omega a^2 t$ (a non-dimensional time), the solution is sought by way of a perturbation series depending on two timescales (see Guckenheimer & Holmes 1983, chap. 4 and references therein):

$$\left.\begin{aligned}\eta(\theta,t)&=A(\theta,t)\,\mathrm{e}^{\frac{1}{2}\mathrm{i}\omega t}+\text{c.c.},\\ A(\theta,t)&=\sum_{m=1}^{\infty}a_m(t)\,\mathrm{e}^{\mathrm{i}m\theta}\\ &=A_0(\theta,\tau)+aA_1(\theta,t,\tau)+a^2A_2(\theta,t,\tau)+\ldots,\\ \frac{\partial A}{\partial t}&=a\frac{\partial A_1}{\partial t}+a^2\left(\frac{\partial A_2}{\partial t}+\omega\frac{\partial A_0}{\partial\tau}\right)+\ldots,\end{aligned}\right\} \tag{A 8}$$

where the A_k, like A, are expressed as sums over positive m. This choice of decomposition automatically satisfies (A 7) at the lowest order. At $O(a)$, (A 7) yields

$$\frac{1}{\omega}\frac{\partial A_1}{\partial t}\mathrm{e}^{\frac{1}{2}\mathrm{i}\omega t}=\tfrac{1}{2}z_0\left(A_0\frac{\partial A_0}{\partial\theta}\mathrm{e}^{\mathrm{i}\omega t}+\frac{\partial W_0}{\partial\theta}\right), \tag{A 9}$$

where $W_0(\theta,\tau)$ is the part of $|A_0|^2$ involving only the spectral series in positive m. Equation (A 9) has the particular solution

$$A_1=\mathrm{i}z_0\left(\frac{\partial W_0}{\partial\theta}\mathrm{e}^{-\frac{1}{2}\mathrm{i}\omega t}-A_0\frac{\partial A_0}{\partial\theta}\mathrm{e}^{\frac{1}{2}\mathrm{i}\omega t}\right). \tag{A 10}$$

The homogeneous solution could be a general function of θ and τ, but for reasons of initialization discussed below, it is set to zero (this is equivalent to absorbing the homogeneous solution into the definition of A_0).

At $O(a^2)$, (A 7) yields two equations, one for the evolution of A_2 (on the timescale

t) and the second for the evolution of A_0 (on the timescale τ). The second equation results from equating terms that would otherwise lead to secular growth of A_2, terms proportional to $e^{\frac{1}{2}i\omega t}$ and expressible as a series in $e^{im\theta}$ for positive m. This equation is

$$\left.\begin{aligned} &\frac{\partial A_0(\theta,\tau)}{\partial\tau} = \frac{\partial B_0}{\partial\theta}, \\ &B_0(\theta,\tau) = \tfrac{1}{2}iz_0^2\left(A_0\frac{\partial}{\partial\theta}(W_0 - W_0^*) - |A_0|^2\frac{\partial A_0}{\partial\theta}\right) - \tfrac{1}{2}(z_0^2+1)\,|A_0|^2 A_0 \\ &\qquad - \frac{1}{8\pi}\int_0^{2\pi} d\alpha \frac{|A(\alpha,\tau)-A(\theta,\tau)|^2[A(\alpha,\tau)-A(\theta,\tau)]}{1-\cos(\alpha-\theta)}, \end{aligned}\right\} \quad \text{(A 11)}$$

where only the part of B_0 expressible as $\sum_{m=1}^{\infty} b_{0m}(\tau)\, e^{im\theta}$ is intended. Equivalently, the spectral coefficients $a_m(\tau)$ of A_0 (dropping the subscript 0 for notational simplification) satisfy

$$\frac{da_m}{d\tau} = \tfrac{1}{4}im \sum_{n,p}^{\infty} a_n a_p a^*_{n+p-m}[n+p-|n-m|-|p-m|-2+2z_0^2(n+p-m-1)], \quad \text{(A 12)}$$

where the double sum is constrained by $n+p > m$.

In numerical calculations, (A 12) requires $O(M^3)$ operations per time step if only the first M coefficients are kept, whereas a pseudospectral method for (A 11) described next requires only $O(M^2)$ operations. In the pseudospectral method, the right-hand side of (A 11) is evaluated on a mesh of $2M$ equally spaced points in θ using centred differences wherever derivatives appear, and the result is then transformed to give the evolution (through a fourth-order Runga–Kutta method with time step $\Delta\tau = 1/(2\pi)$) of the $M = 1024$ spectral coefficients. This transform has the effect of saving only that part of the right-hand side of (A 11) having a series in positive m. Similarly, a transform of $|A_0|^2$ yields the spectral coefficients of W_0 and therefore W_0 itself.

Initialization of (A 11) is accomplished as follows. The spectral coefficients of $A(\theta,0)$ are supplied by the transform of the given initial condition $\eta(\theta,0)$, and $A_0(\theta,0)$ is obtained by the following symbolic inversion:

$$\text{known} \to A = A_0 + aA_1[A_0] + \ldots, \quad \text{(A 13)}$$

with the functional dependence of A_1 on A_0 set by (A 10) at $t = 0$. The solution for A_0 may then be obtained in the form of a perturbation series,

$$A_0 = A - aA_1[A] + O(a^2), \quad \text{(A 14)}$$

and in this paper, owing to the great complexity of the quadratic-order term, only the first two terms in (A 14) are used. As a result, the calculations in figures 11 and 12 suffer from observably imperfect initialization, yet they nevertheless capture many aspects of the fully nonlinear evolution.

Appendix B. The evolution of a localized disturbance on a vorticity interface

Fully nonlinear numerical calculations of the kind illustrated in this paper cannot determine whether or not an arbitrarily shallow disturbance will eventually

commence filamentation. The equations of motion are simply too difficult to solve accurately. Instead, by assuming that the disturbance is confined to only a small part of the vortex boundary, it is possible to reduce the problem to that of a disturbance to an infinite interface of vorticity. These 'localized' equations, derived in the first part of this appendix, are no less nonlinear than the original equations of motion but do let one consider an arbitrarily small disturbance. The steepening process is isolated by further assuming that the disturbance is shallow, expanding the localized equations in a perturbation series, and performing a two-timescales analysis. The result of this exercise, the thrust of the second part of this appendix, is a universal equation governing the steepening of arbitrarily shallow, localized disturbances propagating on general vorticity interfaces.

B.1. *The localized equations*

Contour dynamics was named for the following property of a piecewise-constant vorticity distribution: the boundaries of vorticity discontinuity or 'contours' alone determine the velocity at *any* point in the fluid. The evolution of the contours depends only on the positions of and the jumps in vorticity across the contours. For a single vortex patch embedded in unbounded irrotational fluid, the velocity at a point $\boldsymbol{x}$ is

$$\boldsymbol{u} = -\frac{\omega}{4\pi}\oint_C \log\|\boldsymbol{x}-\boldsymbol{x}'\|^2\,\mathrm{d}\boldsymbol{x}', \tag{B 1}$$

where C denotes the boundary of the vortex traced out by $\boldsymbol{x}'$ with the inside of the vortex on the left of C, and ω is the uniform vorticity within C.

The immediate task is to simplify (B 1) in the case that the contour C differs only slightly from an equilibrium or steady contour $\bar{C}$ over a small part of $\bar{C}$. More precisely, the disturbance to $\bar{C}$ that gives rise to C is assumed to have an amplitude a and extent δ much smaller than the radius of curvature of $\bar{C}$, where C and $\bar{C}$ differ. (It is also assumed, trivially, that the ratio of a to δ is at most order unity.) However, this is *not* sufficient to specify the disturbance; it is also necessary for the disturbance curvature, measured by a/δ^2, to greatly exceed the curvature of the equilibrium contour. This final condition removes the effect of dispersion arising from variations in curvature along the vorticity interface. The need for these conditions is made apparent in the analysis to follow.

To simplify notation, a reference frame is chosen that freezes $\bar{C}$. Arclength s can then be used to identify a point $\bar{\boldsymbol{x}}$ on $\bar{C}$. Let the 'centre' of the disturbance be given by $s = s_0(t)$, where t denotes time. Because the disturbance is localized, its centre may be taken to be a fluid particle on $\bar{C}$ in which case $\mathrm{d}s_0/\mathrm{d}t = \dot{s}_0 = q_0 = \|\bar{\boldsymbol{u}}[\bar{\boldsymbol{x}}(s_0(t))]\|$. In the following, equilibrium quantities evaluated at s_0 are subscripted by '0' with the bar removed, e.g. $\boldsymbol{x}_0(t) = \bar{\boldsymbol{x}}[s_0(t)]$.

Next, a right-handed Cartesian coordinate system (ξ, η) centred on $\boldsymbol{x}_0$ is introduced. The positive ξ-axis is directed tangent to $\bar{C}$ (in the direction of *decreasing* s), and the positive η-axis points normally outward. The coordinate transformation is defined by the unit tangent and normal vectors, $\hat{\boldsymbol{t}}_0$ and $\hat{\boldsymbol{n}}_0$, at $s = s_0(t)$ (see figure 15)

$$\xi = -\hat{\boldsymbol{t}}_0\cdot(\boldsymbol{x}-\boldsymbol{x}_0), \quad \eta = \hat{\boldsymbol{n}}_0\cdot(\boldsymbol{x}-\boldsymbol{x}_0). \tag{B 2}$$

Taking a time derivative of (B 2) and then replacing $\boldsymbol{x}-\boldsymbol{x}_0$ by $-\xi\hat{\boldsymbol{t}}_0+\eta\hat{\boldsymbol{n}}_0$ yields

$$\dot{\xi} = -\hat{\boldsymbol{t}}_0\cdot(\boldsymbol{u}-\boldsymbol{u}_0)+\lambda\eta, \quad \dot{\eta} = \hat{\boldsymbol{n}}_0\cdot(\boldsymbol{u}-\boldsymbol{u}_0)-\lambda\xi, \tag{B 3}$$

where $\lambda = \hat{\boldsymbol{t}}_0\cdot\mathrm{d}\hat{\boldsymbol{n}}_0/\mathrm{d}t = q_0\kappa_0$, κ_0 being the curvature along the equilibrium vortex at

the centre of the disturbance. λ is the rotation rate of the transformed coordinate system.

Assume next that the point $\boldsymbol{x}$ is on C. It remains to express $\boldsymbol{u}-\boldsymbol{u}_0$ in terms of the transformed coordinates. $\boldsymbol{u}(\boldsymbol{x})-\boldsymbol{u}_0$ can be rewritten as $\Delta\boldsymbol{u}_1+\Delta\boldsymbol{u}_2$ with $\Delta\boldsymbol{u}_1 = \boldsymbol{u}(\boldsymbol{x})-\bar{\boldsymbol{u}}(\boldsymbol{x})$ and $\Delta\boldsymbol{u}_2 = \bar{\boldsymbol{u}}(\boldsymbol{x})-\bar{\boldsymbol{u}}(\boldsymbol{x}_0)$. $\Delta\boldsymbol{u}_1$ is the difference between the perturbed and equilibrium velocity at $\boldsymbol{x}$, while $\Delta\boldsymbol{u}_2$ is the difference between the equilibrium velocity at $\boldsymbol{x}$ and $\boldsymbol{x}_0$.

First consider the simplification of $\Delta\boldsymbol{u}_1$. Since C and $\bar{C}$ differ negligibly except very near $\boldsymbol{x}_0$, $\Delta\boldsymbol{u}_1$ depends only upon the contour segment C_1 and the very nearly flat segment $\bar{C}_1$ shown in figure 15. Along C_1, $\boldsymbol{x}'-\boldsymbol{x}_0 = -\xi'\hat{\boldsymbol{t}}_0+\eta'\hat{\boldsymbol{n}}_0$, while along $\bar{C}_1$, $\bar{\boldsymbol{x}}-\boldsymbol{x}_0 \approx -\bar{\xi}\hat{\boldsymbol{t}}_0$, so that

$$\Delta\boldsymbol{u}_1 = \frac{\omega}{4\pi}\int_{C_1}\log[(\xi-\xi')^2+(\eta-\eta')^2]\{-\hat{\boldsymbol{t}}_0\,\mathrm{d}\xi'+\hat{\boldsymbol{n}}_0\,\mathrm{d}\eta'\} - \frac{\omega}{4\pi}\int_{\bar{C}_1}\log[(\xi-\bar{\xi})^2+\eta^2]\{-\hat{\boldsymbol{t}}_0\,\mathrm{d}\bar{\xi}\}, \tag{B 4}$$

a sign change coming from reversing the direction of the contour integrations.

Finally, consider $\Delta\boldsymbol{u}_2 = \bar{\boldsymbol{u}}(\boldsymbol{x})-\bar{\boldsymbol{u}}(\boldsymbol{x}_0)$. Define $\bar{\mu}(\xi,\eta) = -\hat{\boldsymbol{t}}_0\cdot\bar{\boldsymbol{u}}(\boldsymbol{x})$ and $\bar{\nu}(\xi,\eta) = \hat{\boldsymbol{n}}_0\cdot\bar{\boldsymbol{u}}(\boldsymbol{x})$. $\bar{\mu}$ and $\bar{\nu}$ are the velocity components parallel to the ξ- and η-axes respectively. Then to first order in a Taylor series expansion,

$$\left.\begin{aligned} -\hat{\boldsymbol{t}}_0\cdot\Delta\boldsymbol{u}_2 &= \bar{\mu}(\xi,\eta)-\bar{\mu}(0,0) = \xi\frac{\partial\mu_0}{\partial\xi}+\eta\frac{\partial\mu_0}{\partial\eta},\\ \hat{\boldsymbol{n}}_0\cdot\Delta\boldsymbol{u}_2 &= \bar{\nu}(\xi,\eta)-\bar{\nu}(0,0) = \xi\frac{\partial\nu_0}{\partial\xi}+\eta\frac{\partial\nu_0}{\partial\eta}. \end{aligned}\right\} \tag{B 5}$$

The higher-order terms in the Taylor series involve products of the small parameters $a\kappa_0$, $\delta\kappa_0$, and $\delta^2\kappa_0/a$ (assuming that $\partial^{m+n}(\mu_0,\nu_0)/\partial^m\xi\,\partial^n\eta$ scales as $\omega\kappa_0^{m+n-1}$, $m+n\geqslant 2$) as do the neglected terms in (B 4) above.

The equilibrium velocity gradients are related by a continuity equation and a vorticity equation:

$$\frac{\partial\mu_0}{\partial\xi}+\frac{\partial\nu_0}{\partial\eta} = 0, \quad \frac{\partial\nu_0}{\partial\xi}-\frac{\partial\mu_0}{\partial\eta} = \bar{\omega}, \tag{B 6}$$

where $\bar{\omega} = \omega-2\Omega$ if $\eta<0$, $\bar{\omega} = -2\Omega$ if $\eta>0$, and Ω is the rotation rate of the reference frame in which $\bar{C}$ is stationary. Because the transformed coordinate axes are rotating at the rate λ, $\partial\nu_0/\partial\xi = \lambda$. The vorticity equation then gives $\partial\mu_0/\partial\eta = \lambda-\bar{\omega}$. Defining the 'along-contour strain' γ by

$$\gamma = \frac{\partial\mu_0}{\partial\xi} = \frac{\mathrm{d}\bar{\boldsymbol{x}}}{\mathrm{d}s}\cdot\frac{\mathrm{d}\bar{\boldsymbol{u}}}{\mathrm{d}s} \quad \text{at } s = s_0(t), \tag{B 7}$$

continuity implies $\partial\nu_0/\partial\eta = -\gamma$. Equation (B 3) can now be expressed entirely in terms of the transformed coordinates:

$$\left.\begin{aligned} \dot{\xi} &= \frac{\omega}{4\pi}\int_{C_1}\{\log[(\xi-\xi')^2+(\eta-\eta')^2]-\log[(\xi-\xi')^2+\eta^2]\}\,\mathrm{d}\xi'+\gamma\xi+(2\lambda-\bar{\omega})\,\eta,\\ \dot{\eta} &= \frac{\omega}{4\pi}\int_{C_1}\log[(\xi-\xi')^2+(\eta-\eta')^2]\,\mathrm{d}\eta'-\gamma\eta. \end{aligned}\right\} \tag{B 8}$$

Upon scaling ξ and η by the small extent of the disturbance, these equations can be rewritten in a more revealing form after making use of the following relation:

$$-\frac{\omega}{4\pi}\int_{C_1}\{\log[(\xi-\xi')^2+\eta^2]-\log[\xi-\xi']^2\}\,\mathrm{d}\xi' = -\frac{\omega}{4\pi}\int_{-\infty}^{\infty}\{\log[\tilde{\xi}^2+\eta^2]-\log\tilde{\xi}^2\}\,\mathrm{d}\tilde{\xi}$$
$$= -\tfrac{1}{2}\omega|\eta|. \tag{B 9}$$

With the further definition $\alpha(t) = 2\lambda(t)+2\Omega-\tfrac{1}{2}\omega,$ (B 10)

the localized equations in final form are

$$\left.\begin{aligned}\dot{\xi} &= \frac{\omega}{4\pi}\int_{C_\infty}\{\log[(\xi-\xi')^2+(\eta-\eta')^2]-\log[\xi-\xi']^2\}\,\mathrm{d}\xi'+\gamma\xi+\alpha\eta,\\ \dot{\eta} &= \frac{\omega}{4\pi}\int_{C_\infty}\log[(\xi-\xi')^2+(\eta-\eta')^2]\,\mathrm{d}\eta'-\gamma\eta,\end{aligned}\right\} \tag{B 11}$$

where C_∞ is an infinite curve extending from $\xi = -\infty$ to ∞ for which η tends to zero for large $|\xi|$.

B.2. *Extensions to more general vorticity distributions*

Equations virtually identical to those just derived apply equally well to non-equilibrium conditions and to general piecewise-constant vorticity distributions. If the contour $\bar{C}$ surrounding a single patch of vorticity is unsteady, the concept of disturbance can still be defined as long as there is a spatial and temporal scale separation between the disturbance and the basic flow. In other words, the extent of the disturbance is assumed to be much smaller than the radius of curvature of $\bar{C}$ at the position of the disturbance, and the frequency of oscillation of the disturbance much greater than the rate at which changes are taking place to the large-scale structure of the supporting interface. The only changes to (B 11) are in the definitions of λ and γ: $\lambda = \hat{\boldsymbol{t}}_0\cdot\mathrm{d}\hat{\boldsymbol{n}}_0/\mathrm{d}t$ no longer equals $q_0\kappa_0$; γ in (B 7) is instead defined in terms of partial derivatives with respect to arclength, and arclength is measured from the location of the centre of the disturbance, $\boldsymbol{x}_0(t)$.

If, in addition, there exists more than one contour (a general piecewise-constant vorticity distribution), then as long as the disturbance is much smaller than the distance between contours, a disturbance on any one contour obeys (B 11) with a minor change in the definition of α: $\alpha = 2\lambda-\tfrac{1}{2}(\omega_\mathrm{i}+\omega_\mathrm{o})$, where ω_i is the vorticity just inside the contour, and ω_o is that just outside.

Finally, (B 11) holds even for generally curved two-dimensional surfaces with or without boundaries. Green's function will no longer be proportional to the logarithm of distance (except on the surface of a sphere), but the result (B 11) depends only on the local behaviour of Green's function which, for sufficiently small disturbances, *is* always proportional to the logarithm of distance. For the same reasons, (B 11) continues to apply to piecewise-constant vorticity flows for which the vorticity is related to the stream function via Helmholtz's equation ($\omega = \nabla^2\psi+\lambda^2\psi$) or even for axisymmetric flow (Shariff 1988) as long as the disturbance does not lie upon the axis of symmetry (for when it does, see Moffatt & Moore 1978).

B.3. *Weakly nonlinear theory*

Not only does the restriction to infinitely localized disturbances prove vital to the derivation of (B 11), but it also endows (B 11) with the equal-frequency property

necessary for the derivation of an envelope equation evolving on a long timescale. The derivation qualitatively parallels that given in Appendix A but with new twists associated with variable strain and shear.

First, (B 11) is expanded in a perturbation series in wave slope. Equivalently, since the disturbance is assumed to have $O(1)$ extent, η is replaced by $\epsilon\eta$, $\epsilon \ll 1$, and, with errors of $O(\epsilon^4)$, (B 11) reduces to

$$\left.\begin{aligned} \dot{\xi} &= \gamma\xi + \epsilon\alpha\eta + \frac{\omega\epsilon^2}{4\pi}\int_{-\infty}^{\infty} \mathrm{d}\xi' \Theta^2, \\ \dot{\eta} &= -\frac{\omega}{2\pi}\int_{-\infty}^{\infty} \frac{\eta(\xi',t)\,\mathrm{d}\xi'}{\xi'-\xi} - \gamma\eta + \frac{\omega\epsilon^2}{4\pi}\int_{-\infty}^{\infty} \mathrm{d}\xi' \Theta^2 \frac{\partial\eta(\xi',t)}{\partial\xi'}, \\ \Theta &= \frac{\eta(\xi',t)-\eta(\xi,t)}{\xi'-\xi}. \end{aligned}\right\} \tag{B 12}$$

Next, the terms $\gamma\xi$ and $\gamma\eta$ are eliminated from the above equations by a coordinate transformation. First, substitute $\eta = \tilde{\eta}[\beta(t)]^{\frac{1}{2}}$ with

$$\beta(t) = \exp\left(-2\int_0^t \gamma(t')\,\mathrm{d}t'\right) \tag{B 13}$$

followed by $\xi = \tilde{\xi}/\beta^{\frac{1}{2}}$, $t = \tilde{t}$ to obtain (after some rearrangement and suppression of tildes)

$$\frac{1}{\omega}\frac{\partial\eta}{\partial t} + \frac{1}{2\pi}\int_{-\infty}^{\infty} \frac{\eta(\xi',t)\,\mathrm{d}\xi'}{\xi'-\xi} = \frac{\partial}{\partial\xi}\left(-\tfrac{1}{2}\epsilon a\eta^2 + \frac{\epsilon^2\beta^2}{12\pi}\int_{-\infty}^{\infty} \mathrm{d}\xi' \frac{[\eta(\xi',t)-\eta(\xi,t)]^3}{(\xi'-\xi)^2}\right), \tag{B 14}$$

where $a(t) = \alpha\beta/\omega$.

As in Appendix A, one next attempts a two-timescale perturbation-series solution, the second timescale $\tau = \omega\epsilon^2 t$ being quadratic in the small parameter ϵ:

$$\left.\begin{aligned} \eta(\xi,t) &= \bar{\eta} + A(\xi,t)\,\mathrm{e}^{\frac{1}{2}\mathrm{i}\omega t} + \text{c.c.}, \\ A(\xi,t) &= \int_0^{\infty} \mathrm{d}k F(k)\,\mathrm{e}^{-\mathrm{i}k\xi} \\ &= A_0(\xi,\tau) + \epsilon A_1(\xi,t,\tau) + \epsilon^2 A_2(\xi,t,\tau) + \ldots, \end{aligned}\right\} \tag{B 15}$$

where $\bar{\eta}$ is the mean value of η and each of the A_k, like A, have 'one-sided' transforms. Equation (B 14) is automatically satisfied at lowest order, and A_1 follows from equating terms at $O(\epsilon)$:

$$A_1 = 2\mathrm{i}\left(A_0\frac{\partial A_0}{\partial\xi}\hat{a}(t)\,\mathrm{e}^{\frac{1}{2}\mathrm{i}\omega t} - \frac{\partial W_0}{\partial\xi}\hat{a}^*(t)\,\mathrm{e}^{-\frac{1}{2}\mathrm{i}\omega t}\right), \tag{B 16}$$

where $W_0(\xi,\tau)$ is the part of $|A_0|^2$ expressible in terms of spectral coefficients with positive wavenumbers k, and

$$\hat{a}(t) = \tfrac{1}{2}\mathrm{i}\omega\,\mathrm{e}^{-\frac{1}{2}\mathrm{i}\omega t}\int^t \mathrm{d}t\, a(t)\,\mathrm{e}^{\frac{1}{2}\mathrm{i}\omega t} \tag{B 17}$$

conveniently equals a if a is constant.

At $O(\epsilon^2)$, the terms in (B 14) that would otherwise lead to secular growth constitute

the equation for A_0. Only the terms proportional to $e^{\frac{1}{2}i\omega t}$ contribute to the equation for $\partial A_0/\partial\tau$, and thus one finds

$$\left.\begin{aligned}\frac{\partial A_0(\xi,t)}{\partial\tau} &= \langle\beta^2\rangle\frac{\partial B_0}{\partial\xi},\\ B_0(\xi,t) &= \tfrac{1}{2}i\sigma\left(A_0\frac{\partial}{\partial\xi}(W_0-W_0^*)-|A_0|^2\frac{\partial A_0}{\partial\xi}\right)\\ &\quad+\frac{1}{4\pi}\int_{-\infty}^{\infty}d\xi'\,\frac{|A_0(\xi',\tau)-A_0(\xi,\tau)|^2(A_0(\xi',\tau)-A_0(\xi,\tau))}{(\xi'-\xi)^2},\end{aligned}\right\}\qquad(B\ 18)$$

where the angled brackets denote 'the constant part of' (constant in t), and

$$\sigma=\frac{4\langle a\hat{a}\rangle}{\langle\beta^2\rangle}.\qquad(B\ 19)$$

Implicit in the definition of the angled brackets is the assumption that the quantities a and β, if not precisely periodic, are at least periodic on the short timescale t; either quantity may take the following general form:

$$c_0(\tau)+\sum_{n=1}^{\infty}c_n(\tau)\,e^{in\Omega(\tau)t},\qquad(B\ 20)$$

in which case the angled brackets are a function of the long timescale τ. This is equivalent to requiring that the supporting interface vary no faster than the evolution of the disturbance envelope; otherwise, secular behaviour would not occur at any order of the perturbation series.

B.4. *An example: the elliptical vortex*

Explicit expressions can be obtained for the strain and the shear when the boundary is elliptical, and from these one can calculate the coefficients $\langle\beta^2\rangle$ and σ. The unusual behaviour of these coefficients described below gives further insight into the weakly nonlinear theory. Indeed, resonant situations can arise for certain values of the eccentricity that force a more rapid steepening – on the timescale ϵt – and such behaviour is not unique to elliptical vortices.

Fluid particles circuit the boundary of an elliptical vortex according to $x=\cos(\theta+\Omega t)$, $y=b\sin(\theta+\Omega t)$ $(0<\theta<2\pi)$ in a frame rotating at the rate $\Omega=\omega b/(1+b)^2$ (Lamb 1932). The coefficients β and a for a small disturbance initially centred on $x=\cos\theta$, $y=b\sin\theta$ may be shown to satisfy

$$\beta=\frac{1+b^2-(1-b^2)\cos 2\theta}{1+b^2-(1-b^2)\cos 2(\theta+\Omega t)},\quad 2a=\frac{4\Omega\beta^2}{\omega}-\left(\frac{1-b}{1+b}\right)^2\beta.\qquad(B\ 21)$$

The effect of these quantities on the evolution of a disturbance is measured by the coefficients $\langle\beta^2\rangle$ and $\langle a\hat{a}\rangle$. The evaluation of $\langle\beta^2\rangle$ is accomplished easily by complex integration, whence

$$\langle\beta^2\rangle=\frac{1+b^2}{2b}\langle\beta\rangle^2,\quad\langle\beta\rangle=\frac{1+b^2-(1-b^2)\cos 2\theta}{2b}.\qquad(B\ 22)$$

On a circular vortex, both $\langle\beta\rangle$ and $\langle\beta^2\rangle$ equal unity. On the ellipse, $\langle\beta\rangle$ equals the average aspect ratio (amplitude:extent) of the disturbance during a complete journey around the boundary starting and ending at the position θ divided by its

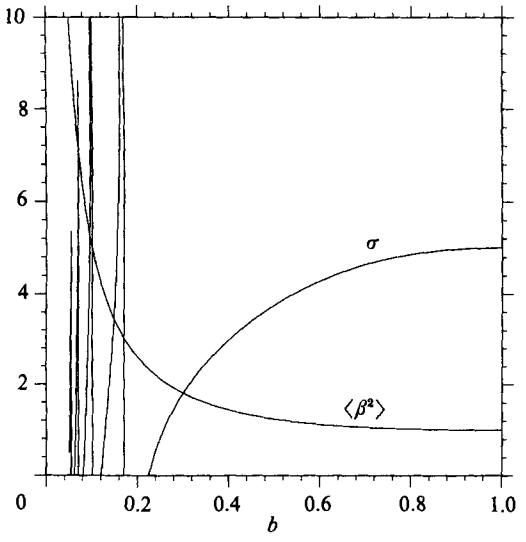

FIGURE 23. The variation of σ and $\langle\beta^2\rangle$ versus b. $b = 1$ corresponds to the circular vortex. σ is singular at an infinite number of values of b accumulating on $b = 0$.

initial aspect ratio. Thus, comparing 'equivalent' disturbances on a circular and an elliptical boundary (disturbances that have the same average aspect ratio over one journey around the vortices), the effect of strain on steepening disturbances, measured by the parameter $\langle\beta^2\rangle$, is greater for elliptical vortices than for circular ones, and the effect increases with the eccentricity of the ellipse.

The curious behaviour stems from the quantity $\langle a\hat{a}\rangle$. Its evaluation is accomplished by first expressing $a(t)$ in the Fourier series

$$a(\phi) = a_0 + \sum_{n=1}^{\infty} a_n (e^{in\phi} + e^{-in\phi}), \quad a_n = \frac{1}{2\pi}\int_0^{2\pi} a(\phi)\cos n\phi \, d\phi, \tag{B 23}$$

where $\phi = 2(\theta + \Omega t)$. Having a series expansion in exponentials, $\hat{a}$ is easily evaluated, and the average assumes the following concise form:

$$4\langle a\hat{a}\rangle = 1 + 8\sum_{n=1}^{\infty} \frac{a_n^2}{1 - n^2\lambda^2}, \tag{B 24}$$

where $\lambda = 4\Omega/\omega = 4b/(1+b)^2$. $\langle\beta^2\rangle$ and $\sigma = 4\langle a\hat{a}\rangle/\langle\beta^2\rangle$ are illustrated in figure 23 (taking $\langle\beta\rangle = 1$). σ *diverges* when the semiminor-axis length $b = b_m$ satisfies $\lambda(b_m) = 1/m$, $m = 2, 3, 4, \ldots$. This is because the mth harmonic of the frequency with which the strain and shear oscillate, 2Ω, resonates with the linear disturbance frequency, $\frac{1}{2}\omega$. Resonance signals secular behaviour in the perturbation-expansion solution to (B 14) occurring at $O(\epsilon)$ rather than at $O(\epsilon^2)$. Near the mth resonance, if one sets $m\lambda = 1 + \epsilon\Lambda$, $\epsilon\Lambda \ll 1$, a re-examination of the multiple-timescales analysis reveals that the envelope of a disturbance evolves on the shorter (but still long) timescale $\zeta = \omega\epsilon t$:

$$\frac{\partial A_0}{\partial\zeta} = -a_m \frac{\partial}{\partial\xi}(W_0 e^{i\Lambda\zeta} + \tfrac{1}{2}A_0^2 e^{-i\Lambda\zeta}), \tag{B 25}$$

where a_m is computed from (B 23) with $b = b_m = 2m - 1 - [(2m-1)^2 - 1]^{\frac{1}{2}}$. For the first few resonant aspect ratios, $b_2 \approx 0.17157$, $a_2 \approx 0.49994$; $b_3 \approx 0.10102$, $a_3 \approx 0.54427$; etc. However, at these aspect ratios, the ellipse is linearly unstable

with a maximal growth rate of nearly 0.2ω (Love 1893; see also Dritschel 1986, §5), and the major disruption to the large-scale flow resulting from this instability is likely to be more important than the steepening of utterly small disturbances before the flow changes significantly (for examples of this disruption, see Dritschel 1986, 1988*b*).

The curious behaviour of σ does not stop with the resonant aspect ratios b_m. When the aspect ratio is very close to unity, the parameter σ is nearly five times greater than the value for a precisely circular vortex (for the circular vortex, the quantity a is exactly one-half while $\beta = 1$ so that σ in (B 19) equals 1). In fact, one must alter, slightly, the derivation of the envelope equation (B 18) when the difference of the aspect ratio from unity is of the order of the disturbance waveslope or smaller. Taking $b = 1-2\epsilon B$ with $B \leqslant O(1)$, one finds first that $\lambda = 1-\epsilon^2 B^2$, and, in (B 23), $a_0 = \frac{1}{2}$, $a_1 = \epsilon B$, and $a_n = O(\epsilon^n)$. Thus, $a(t)$ in (B 14) has the form

$$a(t) = \tfrac{1}{2} + \epsilon B(\mathrm{e}^{\frac{1}{2}\mathrm{i}\omega t}\,\mathrm{e}^{-\mathrm{i}B^2\tau} + \mathrm{e}^{-\frac{1}{2}\mathrm{i}\omega t}\,\mathrm{e}^{\mathrm{i}B^2\tau}) + O(\epsilon^2),$$

and now the perturbation-series solution of (B 14) via (B 15) yields (B 18) with $\sigma = 1$, $\langle\beta^2\rangle = 1$, and the following additional term on the right-hand side of (B 18):

$$-B\frac{\partial}{\partial\xi}(W_0\,\mathrm{e}^{-\mathrm{i}B^2\tau} + \tfrac{1}{2}A_0^2\,\mathrm{e}^{\mathrm{i}B^2\tau}). \tag{B 26}$$

Taking $B \to 0$ in $b = 1-2\epsilon B$, the proper circular vortex limit is recovered. On the other hand, when $1-b$ is small compared with unity but large compared with the disturbance 'waveslope' ϵ, the original equation (B 18) with $\sigma = 5$ then applies. Essentially, the ellipticity factors into the disturbance evolution only when the timescale for the evolution of the disturbance envelope is sufficiently long to experience the accumulative effect of the weak resonance provided by the variation of strain and shear as the disturbance travels around the boundary.

Finally, resonance is not unique to the elliptical vortex. Any equilibria, for which the particle revolution period is an integer multiple of the linear disturbance period, exhibit analogous behaviour.

Appendix C. Periodic planar contour surgery

A periodic version of the planar contour surgery algorithm was used for cases 29 and 30 of table 1. The purpose was to simulate effectively infinitesimal disturbances to the boundary of a circular vortex patch. A periodic algorithm achieves this by assuming that the vortex is disturbed by m identical disturbances around its circumference whose widths δ are much smaller than the separation of adjacent disturbances, $2\pi/m$, in the limit of m tending to infinity. By defining $x = -m\theta$ and $y = m(r-1)$ for one angular span, one arrives at contour-dynamical equations for x-periodic flow (see, e.g. Pullin 1981) with the addition of uniform shear $\frac{1}{2}\omega y$ to the x-velocity component (cf. (B 10) and (B 11)).

The equations are solved most simply by using three coordinates constrained to the surface of a unit cylinder. Indeed, flow on a cylinder satisfies identical contour-dynamical equations. Details of the algorithm will be disclosed in a future publication, and here only the initialization and accuracy of the calculations are discussed.

The two calculations using periodic contour surgery were initialized using the same forms for the disturbance shape as those given in (2) at the beginning of §3 except

that the symbols θ and ρ are replaced with $-x$ and y $(-\pi < x \leqslant \pi)$. Both calculations have $a = \frac{1}{20}$ and $m = 20$ so that the effects of periodicity can be kept at bay. The accuracy of the two calculations are monitored by the accumulative phase error ϵ_C, just as in the infinite-planar and spherical calculations, only ϵ_C now accumulates the errors in the circulation Γ (using $\omega/2\pi$ in place of the vorticity ω, as before). Such a choice is natural because the basic lengthscale for periodic flow is the radius of the cylinder, which is unity here, making Γ a frequency-like quantity.

REFERENCES

DEEM, G. S. & ZABUSKY, N. J. 1978 Vortex waves: stationary V-states, interactions, recurrence, and breaking. *Phys. Rev. Lett.* **40**, 859–862. (Also see Stationary V-states, interactions, recurrence, and breaking. In *Solitons in Action* (ed. K. Longren & A. Scott), pp. 277–293. Academic.)

DRITSCHEL, D. G. 1986 The nonlinear evolution of rotating configurations of uniform vorticity. *J. Fluid Mech.* **172**, 157–182.

DRITSCHEL, D. G. 1988*a* Nonlinear stability bounds for inviscid, two-dimensional, parallel or circular flows with monotonic vorticity, and the analogous three-dimensional quasi-geostrophic flows. *J. Fluid Mech.* **191**, 575–582.

DRITSCHEL, D. G. 1988*b* Contour surgery: a topological reconnection scheme for extended integrations using contour dynamics. *J. Comput. Phys.* **77** (in press).

DRITSCHEL, D. G. 1988*c* Contour dynamics/surgery on the sphere. *J. Comput. Phys.* (in press).

GUCKENHEIMER, J. & HOLMES, P. 1983 *Nonlinear Oscillations, Dynamical Systems, and Bifurcations of Vector Fields*. Springer.

HAYNES, P. H. 1987 On the instability of sheared disturbances. *J. Fluid Mech.* **175**, 463–478.

JUCKES, M. N. & MCINTYRE, M. E. 1987 A high-resolution one-layer model of breaking planetary waves in the stratosphere. *Nature* **328**, 590–596.

LAMB, H. H. 1932 *Hydrodynamics*. Dover.

LOVE, A. E. H. 1893 On the stability of certain vortex motions. *Proc. Lond. Math. Soc.* **25**, 18–34.

MCINTYRE, M. E. & PALMER, T. N. 1983 Breaking planetary waves in the stratosphere. *Nature* **305**, 593–600.

MCINTYRE, M. E. & PALMER, T. N. 1984 The 'surf-zone' in the stratosphere. *J. Atmos. Terr. Phys.* **46**, 825–849.

MCINTYRE, M. E. & PALMER, T. N. 1985 A note on the general concept of wave breaking for Rossby and gravity waves. *PAGEOPH* **123**, 964–975.

MELANDER, M. V., MCWILLIAMS, J. C. & ZABUSKY, N. J. 1987 Axisymmetrization and vorticity-gradient intensification of an isolated two-dimensional vortex through filamentation. *J. Fluid Mech.* **178**, 137–159.

MOFFATT, H. K. & MOORE, D. W. 1978 The response of Hill's spherical vortex to a small axisymmetric perturbation. *J. Fluid Mech.* **87**, 749–760.

PULLIN, D. I. 1981 The nonlinear behaviour of a constant vorticity layer at a wall. *J. Fluid Mech.* **108**, 401–421.

SHARIFF, K. 1988 Ph.D. Thesis in preparation, Dept. of Mech. Engng, Stanford Univ., California, USA.

STERN, M. E. 1985 Lateral wave breaking and shingle formation in large scale shear flow. *J. Phys. Oceanogr.* **15**, 1274–1283.

STERN, M. E. & PRATT, L. J. 1985 Dynamics of vorticity fronts. *J. Fluid Mech.* **161**, 513–532.

THOMSON, W. 1880 Vibrations of a columnar vortex. *Phil. Mag.* **10**, 155–168.

WAN, Y. H. & PULVIRENTI, M. 1985 Nonlinear stability of a circular vortex. *Commun. Math. Phys.* **99**, 435–450.

ZABUSKY, N. J., HUGHES, M. H. & ROBERTS, K. V. 1979 Contour dynamics for the Euler equations in two dimensions. *J. Comput. Phys.* **30**, 96–106.